universität innsbruck

Fabrication and Characterization of Free-Standing Airbridges

MASTER THESIS

by

Deniz Egem Molavali

submitted to the Faculty of Mathematics, Computer Science, and Physics of the University of Innsbruck in partial fullfillment of the requirements for the degree of

Master of Science (MSc)

Innsbruck, August 2025

carried out at the Institute of Experimental Physics
under the supervision of

UNIV.-PROF. DR. GERHARD KIRCHMAIR

Abstract

Grounding is crucial in coplanar superconducting circuit architectures, since chip complexity and scalability increase, asymmetries and discontinuities in the ground plane arise. These irregularities excite parasitic slotline modes, which can be coupled to qubits or other resonant modes and degrade circuit performance. Wirebonds are one of the most frequently used crossovers for grounding—also in *Quanten Nano Zentrum Tirol (QNZT)* — however, due to their size, they introduce large inductive losses and are not practical for large-scale chips.

The small structure of airbridges causes lower inductive losses and is compatible with scalable superconducting devices because the density of airbridges can be increased simply by modifying the fabrication design. In this project, airbridges are fabricated for the first time in the QNZT using a single-step grayscale electron beam lithography technique, inspired by the work of Janzen et al. [1]. To optimize the grayscale electron beam lithography process, special techniques are employed, such as delayed development [2] and 3D proximity effect correction (PEC) [3]. In addition, pure Methyl Isobutyl Ketone (MIBK) is used as the developer. The lower contrast characteristic of the positive resist is achieved by pure MIBK and delayed development, so that this technique increases the precision of the resist height after development. A high temperature reflow process is avoided, which can alter the characteristics of Josephson junctions. In addition, PEC is employed to increase the precision of the lithographic process, which is essential in low acceleration voltage Electron Beam Lithography(EBL). Eventually, we achieved a smooth arc-shaped airbridge mask with over 99% yield for airbridges ranging from 45 μm to 65 μm and over 80% yield for 85 μm airbridges. These structures also demonstrated durability against dicing, ultrasonication and N_2 blow-drying. Finally, two chips with CPW resonators grounded by airbridges are characterized at cryogenic temperatures.

Acknowledgements

First, I want to express my gratitude to my supervisor Prof. Gerhard Kirchmair for accepting me as a master's student and giving me the chance to work on this project, which I really enjoyed. I also feel very lucky to be his student in such a friendly group.

I am grateful to all group members for always being careful, supportive, and kind. Special thanks to Teresa Hönighl-Decrinis—her open-minded questions helped me a lot. Julian Daser, thank you showing me the cleanroom and teaching me the tricks. Without the help of Julian and Teresa, this work would not have been possible.

Lastly, I want to thank all my friends, especially Yusuf and Kutay, who always supported me. My source of motivation and love, Irem, without her, both I and the figures in this thesis would look much less good, so I am thankful for her sense of aesthetics. Very special thanks to my parents for always supporting me.

Contents

CHAPTER 1

Introduction

Over the past hundred years, fundamental research into quantum phenomena has opened new pathways toward potential quantum technologies. In 1982, Richard Feynman proposed the idea of a quantum computer [4]. Since then, quantum computers have been studied on various platforms, such as trapped ions, superconducting qubits, and photonic devices [5–7]. Over the last decade, significant progress has been made towards building functional quantum computers and in 2019, quantum advantage was demonstrated by Arute et al. [8]. Looking forward, the goal is to increase scalability, develop robust quantum error correction [9, 10], and advance quantum algorithms [11, 12], ultimately leading to efficient quantum computers capable of solving complex problems.

Due to their high design flexibility and high coherence time, superconducting qubits are considered one of the most promising platforms for quantum computers [13, 14]. Since the first demonstration of a superconducting qubit in 1999 [6], more than twenty years have passed, and we are now in the Noisy Intermediate-Scale Quantum (NISQ) era [15], where it is possible to control systems with over 50 qubits [16]. Superconducting qubits offer several advantages over other platforms, such as trapped ions and optical systems. These include high designability through fabrication and layout, relatively easy coupling of multiple qubits via inductive or capacitive interactions, and operation using commercially available microwave control devices.

Coplanar waveguide (CPW) resonators play a significant role in circuit quantum electrodynamics (cQED) due to their ability to store single photons and couple coherently to two-level systems [17]. Moreover, CPW resonators are widely used for coherent single-qubit control [17], dispersive qubit readout [18], and coupling of multiple qubits [19]. CPW resonators are easily designable up to frequencies of 10 GHz and beyond, and can exhibit large internal quality factors of the order of 10^5 to 10^6 [20–23]. During this thesis, CPW resonators of varying lengths were designed and fabricated with both half-wavelength and quarter-wavelength geometries, and their properties were characterized using the S_{21} transmission spectrum.

Ideally, the ground plane should have equal potential on both sides of the CPW line. However, as the scale and complexity of superconducting chips increase, asymmetries and discontinuities in the ground plane can lead to parasitic slotline modes. These unwanted modes can be coupled to qubits or resonators and become sources of radiation loss and decoherence [24, 25]. To suppress these modes, the ground plane potential must be equalized. This is achieved using metallic crossovers such as wirebonds [26], dielectric bridges and airbridges [1, 27–35]. Wirebonds are often used to connect the ground plane because they do not require additional fabrication steps and are easy to apply. However, they are not practical for larger-scale chips. In addition, wirebonds have a much higher inductance than airbridges due to their relatively large size and their impedance of approximately 40 Ω makes them inefficient as crossovers in superconducting chips [29]. Dielectric bridges, on the other hand, are metallic crossovers supported by a dielectric layer, unlike airbridges. However, they are also less effective due to the additional shunt capacitance introduced by the dielectric medium, which can be a source of dielectric loss.

Airbridges are the most promising method for crossing the ground plane due to their low loss, on the order of 10^{-8} per airbridge at the single photon level [1, 29, 31]. However, the fabrication of airbridges may introduce additional loss to the circuit and potentially alter the characteristics of Josephson junctions due to the high temperatures typically used in many airbridge fabrication processes. In this thesis, Aluminum airbridges were fabricated for the first time at the QNZT using a single-step grayscale lithography technique, performed at relatively low temperatures. The fabricated airbridges demonstrated over 99% yield for lengths up to 65 μm.

This thesis is structured as follows. Chapter 2 presents the theoretical background of microwave technology, transmission lines and microwave resonators. Design considerations and fabrication details for the CPW resonators are provided in Chapter 3. Chapter 4 reviews the literature on the current airbridge designs and introduces the fundamentals of nanofabrication, with a particular focus on techniques used for airbridge fabrication at the QNZT, such as grayscale e-beam lithography, proximity effect correction and delayed development. The mechanical stability of the fabricated airbridges is also evaluated and SEM images are included. Chapter 5 presents the microwave measurements of the fabricated devices. Finally, Chapter 6 offers conclusions and outlines possible directions for future experiments. A detailed fabrication recipe is provided in the appendix.

CHAPTER 2

Theory

In this chapter, we will discuss the theorotical background of selected topics related in this thesis. First, the physics of transmission lines is discussed. Additionally, microwave resonators more spesifically transmission line resonators are given. Key parameters for understanding the properties of microwave resonators, such as the scattering matrix and quality factors, are also covered.

2.1 Superconductivity

Superconductivity is a quantum phenomenon in which certain materials exhibit zero electrical resistance and perfect diamagnetism when they are cooled below a critical temperature (T_c). Heike Kamerlingh Onnes first noted this unusual behavior in 1911. Bardeen, Cooper and Schrieffer developed what is now known as the BCS theory, which was the first sufficient theory of the superconductivity phenomenon [36, 37]. BCS theory describes that electron pairs —Cooper pairs— cause an indirect attractive interaction mediated by lattice vibrations (phonons) in a superconductor. These pairs enable electrical current to flow without energy loss by means of collective action. A Cooper pair forms a condensate in a new many-body ground state that exhibits bosonic characteristics and possesses a lower energy than the Fermi energy of a single electron. The energy difference between the Fermi energy of a single electron and the ground state energy of the Cooper pair is referred to as the superconducting gap. In addition to its fundamental scientific interest, superconductivity also drives advanced technologies and research areas such as quantum computing with superconducting qubits and circuit quantum electrodynamics (cQED)[6, 8].

2.1.1 Supercurrent

The supercurrent is the result of the movement of electron pairs, which they flow without energy loss, in contrast to individual electrons that experience resistive losses [38]. The current-carrying

capacity of a superconductor is limited by the electron pair-breaking mechanism. As the number of electron pairs decreases, the superconducting state eventually collapses. Near the critical temperature T_c, the critical current density can be estimated using Ginzburg-Landau theory. However, since the experiments in this study are performed well below T_c, more advanced theoretical models are required, as the Ginzburg–Landau approach is no longer valid [39]. A more appropriate solution was introduced by Kupriyanov and Lukichev, who numerically solved the Eilenberger equations for current-carrying states [40].

When the width of the sample exceeds the penetration depth, the current distribution becomes non-uniform. The penetration depth is described as the distance from the surface of a superconductor where the magnetic field drops $1/e$ of the magnetic field at the surface of the superconductor. In the context of thin films, the bulk penetration depth λ is modified to λ^2/d, where d is the thickness of the film, this applies when the penetration depth is greater than the thickness of the film. In dirty superconductors where the coherence length ξ_0 is greater than the mean free path, λ is further modified as

$$\lambda = \lambda_L(0)\sqrt{\frac{\xi_0}{l}} \tag{2.1}$$

where $\lambda_L(0)$ is the London penetration depth at zero kelvin, ξ_0 is the BCS coherence length, which represents the size of a Cooper pair and defines the distance over which the superconducting order parameter returns to its bulk value. and l is the mean free path for elastic scattering. The thin film used for air bridges in this work has a width of $10\,\mu$m and a thickness of 370 nm. The critical current density for a similar thick aluminum film in the dirty limit has been reported as $j_c(0) = 299\,\mathrm{GA/m^2}$ [39]. Using this as a reference, the supercurrent can be estimated. The current density for a dirty superconductor is given by

$$j_c = \frac{j_c(0)}{2\sqrt{2}}\left[1 - \left(\frac{T}{T_c}\right)^2\right]^{3/2} \tag{2.2}$$

where $T = 17\,\mathrm{mK}$ and $T_c = 1.2\,\mathrm{K}$. The resulting current density is approximately $j_c \approx 1.06 \times 10^{11}\,\mathrm{A/m^2}$ and the critical current is given by

$$I_c = j_c \cdot A \tag{2.3}$$

where A is the cross-sectional area of the film. The estimated critical current for the air bridge is approximately 0.392 A, which is quite high and exceeds the measurable range in the current cryogenic setup without increasing the temperature of the stage.

2.2 Coplanar Waveguides

Waveguides are structures that are widely used for transmitting data in the form of electromagnetic waves, such as optical fibers, coaxial cables and coplanar waveguides (CPW). CPW is a planar structure on a chip that consists of three parts: center conductor, slotline gaps and ground planes as indicated in Fig. 2.1. Since all the features are 2D, it can be easily fabricated using photolithography or EBL. Coplanar waveguides are widely used in superconducting circuits to realize microwave control lines and resonators.

To understand microwave measurements and device development process, we will look a bit deeper into transmission line theory and equivalent circuit model, the lumped element description of a resonator, CPW resonators as well as S-parameters.

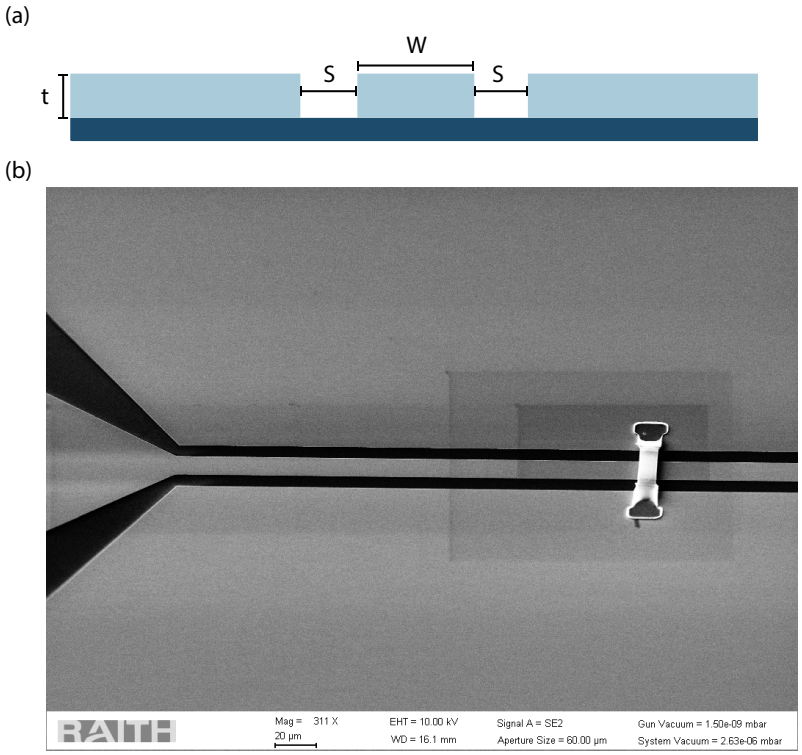

Fig. 2.1 (a) Illustration of CPW geometry. In dark blue is the substrate and light blue areas show the metallic thin film. The t represents the film thickness, s is the slotline gap and w is the width of the central conductor. (b) SEM image of the fabricated CPW transmission line. One can see the bond pad and an airbridge. The dark shadow is an imaging artifact.

2.2.1 Transmission line

High frequency radio waves can be transmitted either with unbounded media like radio broadcast or guided structures such as waveguides. Transmission lines are one of the most common waveguides that are used to transmit electrical signals from one point to another. This and the

following derivations of transmission line theory are adapted from the book by Pozar [41].

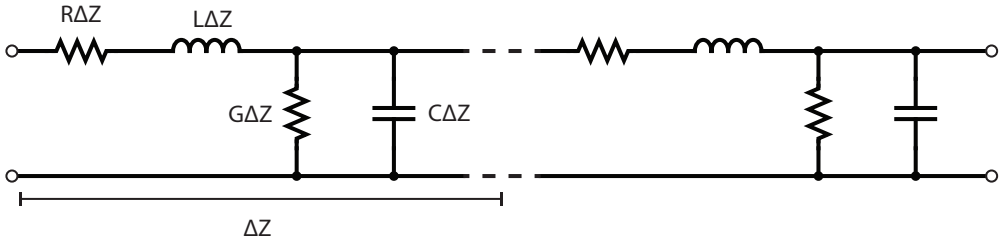

Fig. 2.2 Lumped element equivalent circuit of CPW. R represents the series resistance, L is the self inductance of two conductors, C is the shunt capacitance and G is the shunt conductance per unit length. The figure is remade from [41].

Figure 2.2 shows the equivalent circuit of a transmission line. Here L denotes the self-inductance of the two conductors, C is the shunt capacitance, R is the series resistance due to finite conductivity and G is the shunt conductance representing dielectric loss in the material between the conductors. All parameters are defined per unit length ΔZ. Kirchhoff's voltage law is applied to analyze wave propagation along the transmission line

$$v(z,t) - R\Delta Z\, i(z,t) - L\Delta Z \frac{\partial i(z,t)}{\partial t} - v(z+\Delta Z,t) = 0. \tag{2.4}$$

Additionally, Kirchhoff's current law is applied to the transmission line, resulting in

$$i(z,t) - G\Delta Z\, v(z+\Delta Z,t) - C\Delta Z \frac{\partial v(z+\Delta Z,t)}{\partial t} - i(z+\Delta Z,t) = 0. \tag{2.5}$$

By dividing both equations by ΔZ and taking the limit as $\Delta Z \to 0$, one obtains the following differential equation, known as the Telegrapher's equations [41]

$$\frac{\partial v(z,t)}{\partial z} = -Ri(z,t) - L\frac{\partial i(z,t)}{\partial t}, \tag{2.6}$$

$$\frac{\partial i(z,t)}{\partial z} = -Gv(z,t) - C\frac{\partial v(z,t)}{\partial t}. \tag{2.7}$$

To obtain the wave equations for $I(z)$ and $V(z)$, the two coupled differential equations can be solved.

$$\frac{d^2V(z)}{dz^2} - \gamma^2 V(z) = 0, \tag{2.8}$$

$$\frac{d^2I(z)}{dz^2} - \gamma^2 I(z) = 0. \tag{2.9}$$

Where $\gamma = \alpha + j\beta = \sqrt{(R + j\omega L)(G + j\omega C)}$ is the complex propagation constant. The solution of this second order differential equation is

$$V(z) = V_o^+ e^{-\gamma z} + V_o^- e^{\gamma z}, \tag{2.10}$$

$$I(z) = I_o^+ e^{-\gamma z} + I_o^- e^{\gamma z}. \tag{2.11}$$

The exponential term indicates the wave propagation in the $\pm z$ direction. The characteristic impedance Z_0 is defined as the ratio of voltage to current, given by

$$\frac{V_o^+}{I_o^+} = \frac{-V_o^-}{I_o^-} = Z_0 = \frac{R + j\omega L}{\gamma} = \sqrt{\frac{R + j\omega L}{G + j\omega C}}. \tag{2.12}$$

The voltage can be expressed again in the time domain

$$v(z,t) = |V_o^+| \cos\Big(\omega t - \beta z + \phi^+\Big) e^{-\alpha z} + |V_o^-| \cos\Big(\omega t + \beta z + \phi^-\Big) e^{\alpha z}. \tag{2.13}$$

So far, this discussion has considered a lossy medium, but in many cases, losses in the transmission line can be neglected. For a lossless transmission line, the attenuation constant is $\alpha = 0$ and the phase constant is $\beta = \omega\sqrt{LC}$. In this case, the characteristic impedance is

$$Z_0 = \sqrt{\frac{L}{C}}. \tag{2.14}$$

The wavelength and phase velocity for a lossless transmission line can be expressed as

$$\lambda = \frac{2\pi}{\beta} = \frac{2\pi}{\omega\sqrt{LC}}, \tag{2.15}$$

$$v_p = \frac{\omega}{\beta} = \frac{1}{\sqrt{LC}}. \tag{2.16}$$

2.2.1.1 Terminated lossless Transmission Line

In many cases, the transmission line is terminated with a load impedance or short circuit. In these situations, the power reflected by the load depends on the load impedance Z_L, as illustrated in Fig. 2.3(a).

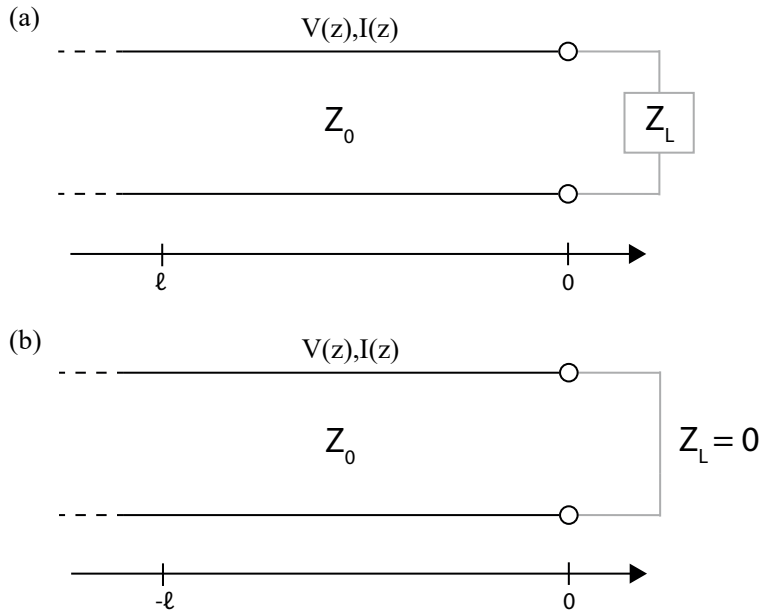

Fig. 2.3 (a) Terminated lossless transmission line a load with impedance Z_L. (b) Transmission line with shorted end. The figure is reproduced from [41].

When a transmission line is terminated with an impedance load Z_L, the current and voltage must satisfy this boundary condition. To achieve this, the reflected wave must have a specific amplitude. The total voltage can be expressed as the sum of the incident and reflected waves

$$V(z) = V_o^+ e^{-j\beta z} + V_o^- e^{j\beta z}, \tag{2.17}$$

$$I(z) = \frac{V_o^+}{Z_0} e^{-j\beta z} - \frac{V_o^-}{Z_0} e^{j\beta z}. \tag{2.18}$$

The load impedance can be determined at the boundary where the load and the transmission line meet, specifically at $z = 0$

$$Z_L = \frac{V(0)}{I(0)} = \frac{V_o^+ + V_o^-}{V_o^+ - V_o^-} Z_0. \tag{2.19}$$

To find the reflection coefficient Γ, this equation can be solved for V_o^-,

$$V_o^- = \frac{Z_L - Z_0}{Z_L + Z_0} V_o^+ \tag{2.20}$$

The ratio between the amplitude and phase of the reflected wave and the incident wave is described with the reflection coefficient

$$\Gamma = \frac{V_o^-}{V_o^+} = \frac{Z_L - Z_0}{Z_L + Z_0}. \tag{2.21}$$

When $\Gamma = 0$, it means that all the power is transmitted with no reflection. This situation occurs when loads are matched $Z_L = Z_0$. On the other hand, when $\Gamma = 1$, indicating that the entire wave is reflected, which indicates a mismatch of the impedances. The input impedance at the beginning of the transmission line, such as at $z = -l$, is given by

$$Z_{\text{in}} = Z_0 \frac{Z_L + jZ_0 \tan \beta l}{Z_0 + jZ_L \tan \beta l}. \tag{2.22}$$

Moreover, when the transmission line is terminated with a short circuit such that $Z_L = 0$ as illustrated in Fig2.3(b), the incident wave is fully reflected back and the reflection coefficient is $\Gamma = -1$. In this case, the incident and reflected waves are in superposition, as described in Eq. 2.18. The input impedance varies along the length of the transmission line with a period of half a wavelength, which shows the presence of these standing waves. Therefore, the input impedance at the $z = -l$ is expressed as

$$Z_{\text{in}} = jZ_0 \tan(\beta l). \tag{2.23}$$

The input impedance oscillates between $+j\infty$ and $-j\infty$.

2.2.2 S-parameter

The scattering matrix (S-matrix) provides information on the transmitted and reflected power within a circuit network. Additionally, it is possible to convert the S-matrix into the impedance matrix Z, which offers a complete picture of the circuit behavior. The following section is adapted from the book by Pozar [42]. For a two-port network, the S-matrix is given as:

$$\begin{pmatrix} V_1^- \\ V_2^- \end{pmatrix} = \begin{pmatrix} S_{11} & S_{12} \\ S_{21} & S_{22} \end{pmatrix} \begin{pmatrix} V_1^+ \\ V_2^+ \end{pmatrix} \tag{2.24}$$

When port j is excited by a voltage V_j^+, the scattering parameter S_{ij} is defined by

$$S_{ij} = \frac{V_i^-}{V_j^+} \,. \tag{2.25}$$

All other ports are terminated in their characteristic impedance to prevent reflections. Hence,

- for $i \neq j$ the procedure yields the *transmission coefficient* S_{ij},
- for $i = j$ it yields the *reflection coefficient* S_{ii}.

For a lossless network, the scattering matrix $\mathbf{S}$ is unitary and its entries are purely imaginary. If the network is also reciprocal, as is typical for structures composed solely of linear, nonmagnetized materials, $\mathbf{S}$ is symmetric, i.e., $S_{ij} = S_{ji}$. Therefore, a reciprocal two-port device can be fully characterized by two independent elements, such as S_{11} and S_{21}. The remaining elements S_{22} and S_{12} are determined by symmetry and unitarity. For a signal on resonance, there will be no transmission in an ideal lossless resonator due to destructive interference of input and reflected waves. In addition, there will be no attenuation off-resonance without any impedance mismatching.

To study microwave resonators, notch or reflection configurations are commonly used. In the notch configuration, as illustrated in Fig. 2.4, a two-port setup is used in which the resonator is capacitively coupled to the transmission line. The transmitted signal is measured and referred to as S_{21}. In the reflection configuration, the same transmission line is used for both input and output: the signal travels to the resonator, reflects back and is measured as S_{11}.

All measurements conducted in this thesis were performed using the notch configuration as shown in Fig.2.4. In the notch configuration, Z_1 and Z_2 represent the impedances of the feedline and the coupling element, respectively, while Z_3 corresponds to the impedance of the resonator. The resonator can be modeled as an RLC circuit, where the resistance R represents a loss channel. These losses are generally categorized as external and internal. For a more comprehensive explanation, including alternative configurations, the thesis by D.Zöpfl [43] is recommended.

2.2.3 Quality Factors

In this section, we discuss the Q-factors to understand the experimental data presented in the results. The Q-factor is proportional to the photon lifetime of a resonator. As the Q-factor increases, the photon lifetime also increases. The quality factor describes the general losses per cycle relative to the energy stored in a resonator [44, 45]. The quality factor of a resonant circuit is defined as

$$Q = 2\pi \frac{\text{average energy stored in resonator}}{\text{energy dissipated per cycle}} = \frac{\omega_r}{\Delta\omega_r} \tag{2.26}$$

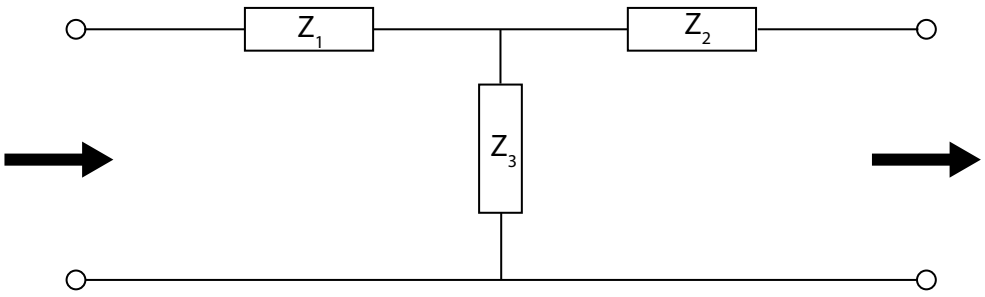

Fig. 2.4 Model of a resonator coupled to a transmission line in a notch configuration. The Z_1 and Z_2 represent the impedance of the transmission line, and Z_3 is the resonator.

Here, $\Delta\omega_r$ is related to the damping of the system that corresponds to the full width half maximum (FWHM) and ω_r is the resonance frequency. The quality factor is a dimensionless number that includes information about the energy loss at the resonator. Moreover, the total quality factor Q_l can be written in two terms, internal and external (also known as coupling quality factor "Q_c") as below,

$$\frac{1}{Q_l} = \frac{1}{Q_c} + \frac{1}{Q_i}. \tag{2.27}$$

The coupling quality factor Q_c is a complex quantity that accounts for both coupling losses and the phase shift due to impedance mismatch [44]. Since it describes energy losses to the external circuitry, Q_c can be tuned through the geometry of the circuit. On the other hand, the internal quality factor Q_i arises from dissipative losses related to intrinsic properties of the resonator, such as material choice and fabrication-induced imperfections. Moreover, the relation between Q_i and Q_c defines three different coupling regimes, as summarized in Table 2.1.

$Q_c \approx Q_i$	critically coupled
$Q_c \gg Q_i$	under-coupled
$Q_c \ll Q_i$	over-coupled

Tab. 2.1 Coupling regimes based on the relationship between Q_c and Q_i.

In the under-coupled regime, most of the losses originate from the internal dissipation of the resonator. In contrast, in the over-coupled regime, energy loss is due to radiation into the waveguide. In the critical coupling regime, the internal and external loss channels contribute approximately equally.

Finally, the transmission coefficient S_{21} can be written in terms of coupling and total quality factor [43]

$$S_{21} = 1 - \frac{Q_l/Q_c}{1 + 2iQ_l\frac{\omega-\omega_r'}{\omega_r'}}. \tag{2.28}$$

These quality factors can be extracted from the transmission measurement using the circle fit routine. Details on the circle fit routine can be found in [43, 46].

2.2.4 Microwave Resonators

Standing waves can exist in a microwave resonator as a result of energy oscillating between the inductive and capacitive elements of the circuit. Alternatively, properties of standing waves, such as wavelength, can be described in terms of the length of the resonator and the boundary conditions of the resonator. For example, a coplanar waveguide (CPW) resonator with two open ends corresponds to a $\lambda/2$ resonator, while one with a single open end corresponds to a $\lambda/4$ resonator, where λ is the wavelength at the resonance frequency.

Before explaining the CPW architecture in detail, we first consider a basic harmonic oscillator—the LC circuit—as illustrated in Fig. 2.5.

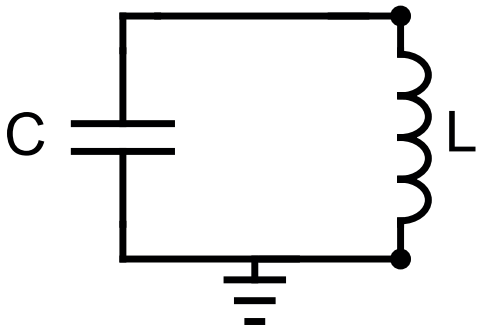

Fig. 2.5 Circuit schematic of an LC circuit. L and C are the inductance and capacitance, respectively.

Like in the classical pendulum, the electrical energy will oscillate between kinetic energy and potential energy

$$T = \frac{C}{2}\dot{\Phi}^2, \tag{2.29}$$

$$U = \frac{\Phi^2}{2L}. \tag{2.30}$$

Here, T and U represent the energies stored in the capacitor and inductor, respectively. The magnetic flux is given by $\Phi = LI$. From equations 2.29 and 2.30, the Lagrangian can be written as

$$L = T - U = \frac{C}{2}\dot{\Phi}^2 - \frac{\Phi^2}{2L} \tag{2.31}$$

The Euler-Lagrange equation can be derived from the Lagrangian.

$$C\ddot{\Phi} + \frac{\Phi}{L} = 0 \tag{2.32}$$

where the angular frequency is given by $\omega = \frac{1}{\sqrt{LC}}$ as follows from the differential equation.

2.2.5 $\lambda/2$ Transmission Line Resonator with Two Open Ends

A CPW resonator with two open ends has a fundamental resonance at $\lambda/2$ [41]. The design details and coupling parameters will be discussed in more detail in the next chapter. The CPW resonator is capacitively coupled to the feedline, as illustrated in Fig. 2.6 and its resonance frequency appears in the transmission or reflection spectrum as a Lorentzian peak. Depending on the geometry of the CPW and the properties of the material, the resonance frequency is given by

$$f_0 = \frac{c}{\sqrt{\epsilon_{\text{eff}}}} \cdot \frac{1}{2l}. \tag{2.33}$$

Here, l is the length of the resonator and ϵ_{eff} is the effective permittivity of the CPW, which also determines the phase velocity. This phase velocity can alternatively be expressed in terms of inductance L and capacitance C, as discussed previously. In general, the total inductance L is the sum of the geometric inductance (temperature-independent) and the kinetic inductance (temperature-dependent), which arises due to the inertia of moving Cooper pairs [22].

Voltage and current are distributed along the transmission line resonator, and the input impedance is given below [41]

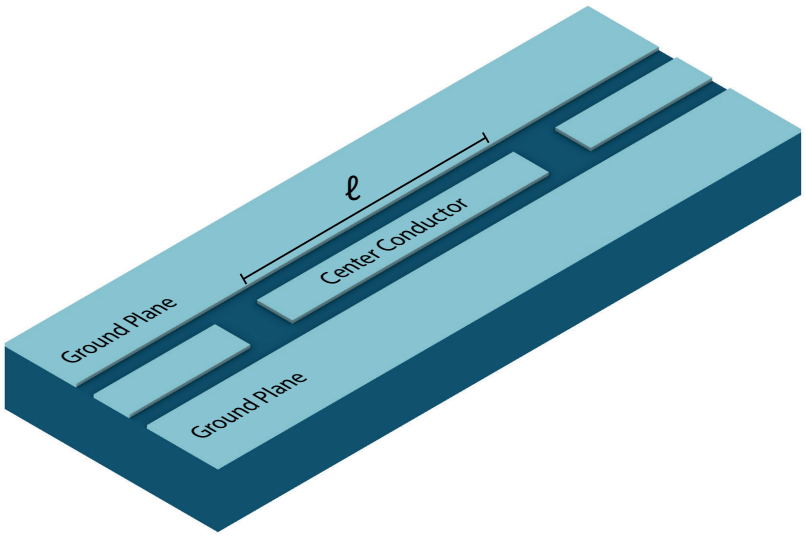

Fig. 2.6 A $\lambda/2$ transmission line resonator of length l, with both ends open, is coupled to a feedline.

$$Z_{\text{in}} = Z_0 \frac{1 + i \tan \beta l \tanh \alpha l}{\tanh \alpha l + i \tan \beta l} \approx \frac{Z_0}{\alpha l + i \frac{\pi}{\omega_0}(\omega - \omega_0)}. \tag{2.34}$$

The α is the attenuation constant, β is the propogation constant and Z_0 is the characteristic impedance. The approximation is valid for ω around the resonance frequency and small loss, such as $\tanh \alpha l \simeq \alpha l$.

CHAPTER 3

Coplanar Waveguide Resonator

In this chapter, we will primarily discuss the design considerations of the CPW geometry, resonator coupling and the fabrication method for CPW using photolithography. The purpose of the simulation is to determine the resonance frequencies and coupling quality factors, which are used to decide on specific parameters such as the coupling length and the gap between the transmission line and the resonator. All simulations were performed using Ansys HFSS [47].

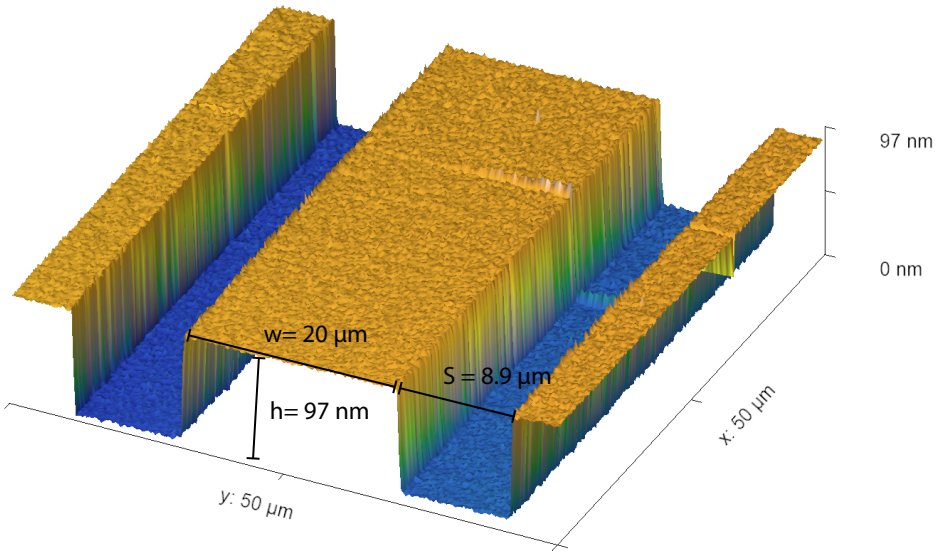

Fig. 3.1 Atomic force microscopy (AFM) image of a fabricated CPW section.

3.1 Design and Simulations

The width of the center trace and the gaps are chosen so that it is a matched 50 Ω transmission line on a sapphire substrate, as shown in Fig. 3.1, to ensure impedance matching with coaxial cables. After deciding on the geometry of the CPW specifically, the resonators are capacitively

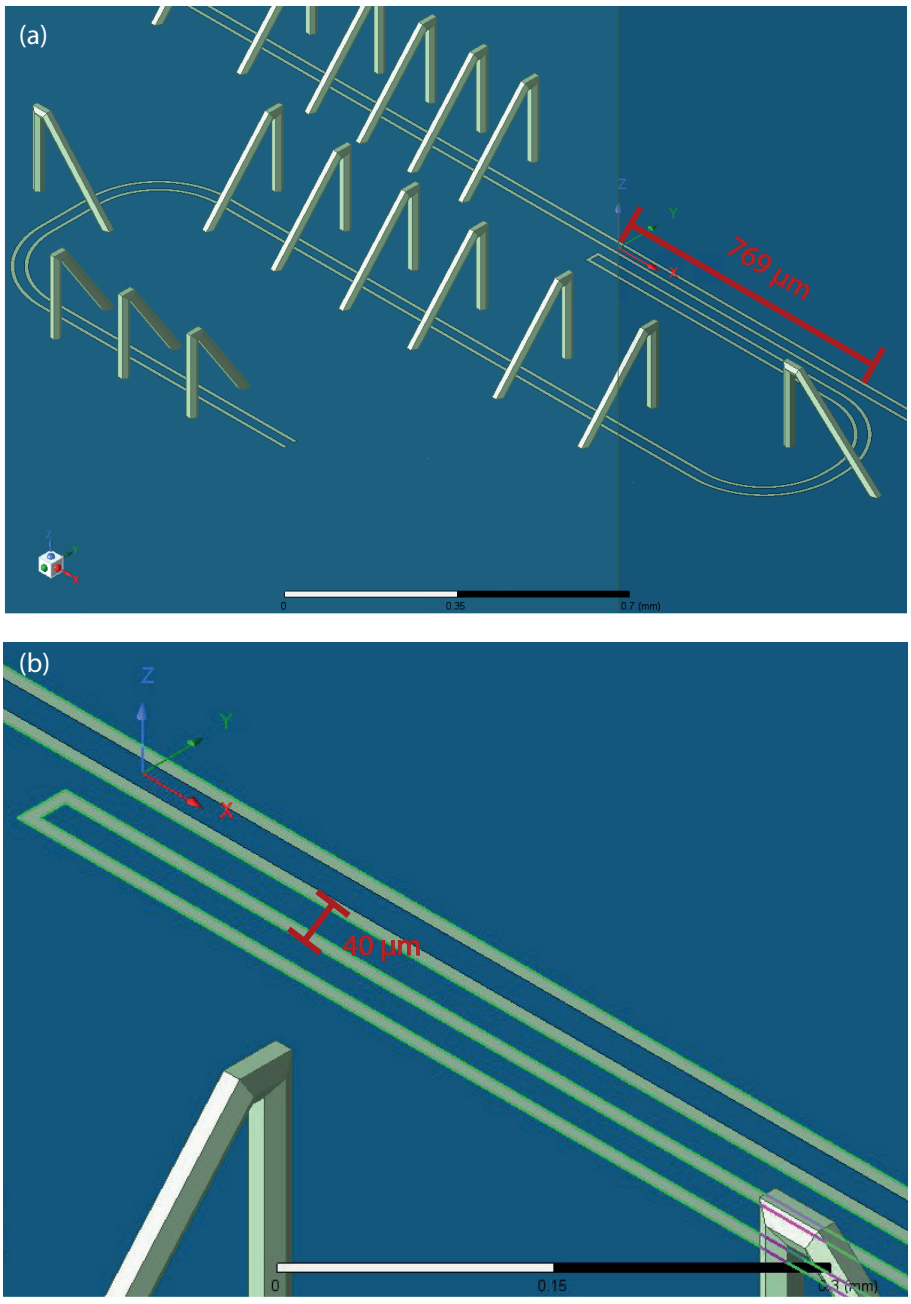

Fig. 3.2 (a)HFSS simulation layout with the resonator coupled to the feedline with two ports with 769μm coupling length. (b) Coupling between the resonator and the feedline with 40μm coupling gap.

coupled to the lossless transmission line as shown in Fig. 3.2. Two parameters can be adjusted

to tune the coupling between the CPW resonator and the transmission line. The first is the coupling length, which refers to the part of the resonator that runs parallel to the feedline, as indicated by the red bar in Fig. 3.2(a). The second is the coupling gap, which is the distance between the center traces of the transmission line and resonator as seen in Fig. 3.2(b). These parameters are varied in the simulation to find the optimal values. In the simulation, the resonator is modeled as being coupled to a two-port transmission line, as shown in Fig. 3.2(a), to obtain the transmission spectrum S_{21}. To extract Q factors and resonant frequencies, the circle fitting routine is applied to S_{21} data.

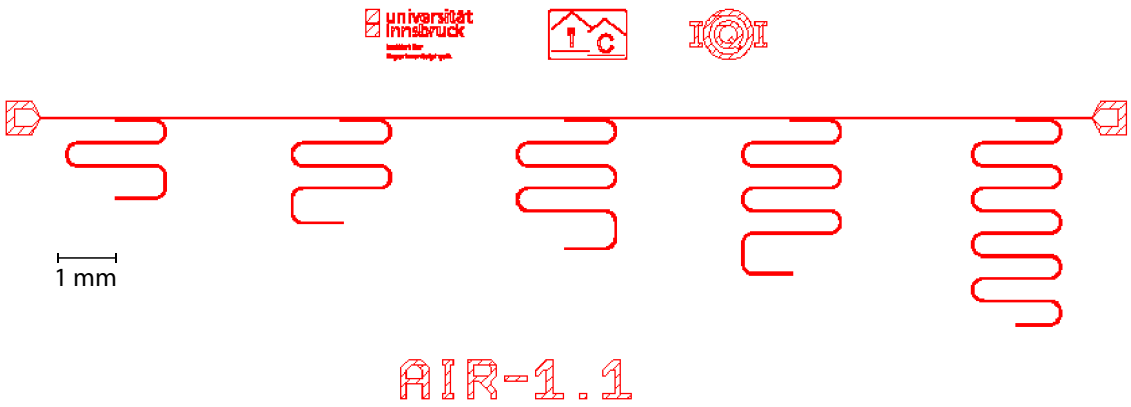

Fig. 3.3 AIR-1 chip outline of the AIR-1 with various lengths of $\lambda/2$ resonator coupled capacitively to the transmission line.

Before fabricating airbridges on CPWs, the first step is to design the chip that includes resonators with different lengths and consequently different resonance frequencies. This chip is called AIR-1, as shown in Figure 3.3. The design contains a transmission line and five $\lambda/2$ resonators with lengths of 6, 8, 10, 12 and 16 mm, each with a 30 μm coupling gap and corresponding coupling lengths of 759, 756, 751, 749 and 655 μm, respectively. The main purpose of the AIR-1 chip is to determine the effective speed of light of a CPW on a sapphire substrate, which is useful for future design iterations.

To investigate the effect of the coupling between the resonator and the transmission line, the coupling length was kept constant while the gap was varied, as shown in Table 3.1 (first four rows). An increase in the coupling gap leads to a higher Q_c, which indicates weaker coupling. Moreover, an increase in coupling length leads to a reduction in total capacitance, which in turn slightly decreases the frequency, as given by $f = \frac{1}{2\pi\sqrt{LC}}$. The remaining rows correspond to simulations of $\lambda/2$ and $\lambda/4$ resonators with different lengths. As expected, the frequencies of the $\lambda/2$ resonators are approximately twice those of the $\lambda/4$ resonators.

From AIR-1, the effective speed of light can be obtained by fitting the resonance frequencies of resonators with different lengths to the inverse relation $\nu = \frac{c_{\text{eff}}}{2l}$. The extracted effective speed of light from the fit is 0.407 c. With this value, future resonators can be designed more precisely, so

$\lambda/2$ or $\lambda/4$	Resonator length (mm)	Gap (center to center) (μm)	Coupling length (μm)	Frequency (GHz)	Q_c
$\lambda/2$	8	10	754	7.828	310
$\lambda/2$	8	20	754	7.77	2132
$\lambda/2$	8	25	754	7.76	4047
$\lambda/2$	8	30	754	7.73	6869
$\lambda/2$	8	40	754	7.71	16186
$\lambda/2$	3	40	530	20.23	5042
$\lambda/4$	3	40	530	10.15	10431
$\lambda/2$	4	40	769	15.23	4537
$\lambda/4$	4	40	769	7.46	9090
$\lambda/2$	5	40	610	11.88	12567
$\lambda/4$	5	40	610	6.09	18403
$\lambda/2$	6	40	759	10.24	9949
$\lambda/4$	6	40	759	5.12	17173
$\lambda/2$	8	40	752	7.78	14393
$\lambda/4$	8	40	752	3.90	25364

Tab. 3.1 Simulated parameters for $\lambda/2$ and $\lambda/4$ resonators.

that their frequencies are determined by their lengths. More details on microwave measurements for next-generation chips will be discussed in Chapter 5.

After realizing that the 40 μm gap resulted in too much coupling in AIR-2 and AIR-3. This issue should be addressed in future designs by decreasing either the coupling length or further increasing the coupling gap. This solution may lead to an observable increase in Q_c and result in weaker coupling, which is important for accurately extracting the internal loss of the resonator [48]. Additionally, increasing the length of the resonator also affects the coupling quality factor, since the ratio of coupling capacitance to total resonator capacitance decreases as the resonator length increases.

3.2 Fabrication of the Coplanar Waveguides

This section outlines the fundamental fabrication steps required to produce high-quality coplanar waveguides on sapphire substrates. The process includes substrate cleaning and preparation, NbTa thin film deposition, photolithographic pattern transfer and final etching and resist removal. Together, these steps define well-controlled ground planes and transmission lines that provide the basis for the superconducting circuits.

NbTa Deposition on The Substrate

Sapphire is used as the substrate for the corresponding devices, as it offers high resistivity and minimal dielectric losses, all of which make it highly suitable for superconducting circuit applications [49]. The sapphire wafers used in this work have a thickness of 330 μm. First, before starting the coating process, the substrate is cleaned with acetone at 50°C using 130 kHz sonication, followed by sonnicating in isopropanol alcohol(IPA) for 5 minutes and drying with a nitrogen gun.

Hydrofluoric acid (HF), specifically a 2% aqueous solution, is used to clean the substrate before coating it with resist, which is known to improve the coherence time of superconducting

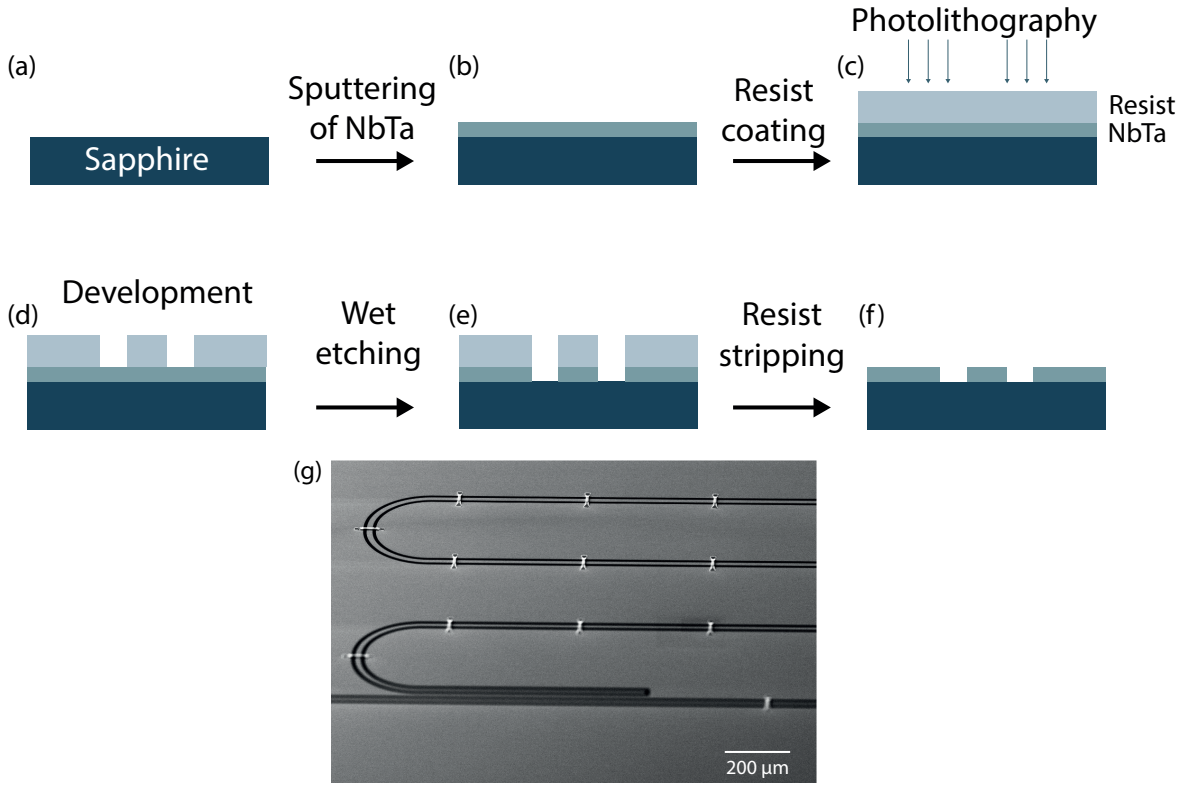

Fig. 3.4 (a-f)Fabrication steps of the CPW: The first image shows the bare wafer, followed by NbTa sputtering, resist coating, photolithography for the CPW mask, wet etching, and finally, resist stripping. (g) Scanning electron microscope image at a tilted angle of the CPW resonator with airbridges.

qubits [50]. After HF treatment, the substrate is rinsed in a DI water bath and then blown dried with a N_2 gun.

After the wafer is cleaned, the NbTa thin film for CPW layout is deposited as soon as possible. As illustrated in Fig. 3.4(b), a 100 nm layer of Niobium (Nb) and a 5 nm layer of Tantalum (Ta) are sputtered using the *AJA ATC-1800* sputtering system. The Ta layer serves as a capping layer to prevent the formation of niobium oxide on the surface, which is known to introduce significant microwave loss [50].

Patern Transfer of The Circuit Layout

Now that the ground plane has been deposited and the wafer is ready for patterning. First, the substrate was cleaned with hot acetone using sonication to remove any potential residue that could degrade the resist coating. Then, it is rinsed in IPA and dried with nitrogen (N_2).

For photolithographic patterning, the wafer is coated in *AZ-1518* photoresist with a resist spinner at 2000 rpm and baked at 90°C for 1 minute on a hot plate (in Fig. 3.4(c)). Since photoresist is sensitive to UV light, special precautions are necessary. It must be handled only in a filtered environment within the cleanroom, commonly referred to as the "yellow room". The door of the

room should remain closed while the resist is open or undeveloped.

After preparation, the wafer was placed on the stage and ready for exposure. The resist is patterned using photolithography, with exposure at a 405 nm wavelength and a dose of 187 mJ/cm^2.

After the exposure is completed, the photoresist remains sensitive to daylight, so the door should be kept closed. A mixture of AZ-developer and deionized (DI) water is prepared in a 1:1 ratio, and the entire wafer is immersed in this developer solution for 90 seconds while being gently shaken to ensure more homogenous development (in Fig. 3.4(d)). During development, the wafer was gently moved to ensure uniform development across the surface.

AZ-developer is a strong base and can be hazardous to the eyes. Therefore, protective goggles are necessary during this step. The development process is stopped by immersing the wafer in DI water for 30 seconds, followed by an additional rinse in fresh DI water to remove any remaining residues. Finally, the wafer is dried with nitrogen (N_2) and the structure is inspected under a microscope to verify that the exposure was successful before proceeding to the hard bake step. The wafer is then hard-baked at 140°C for 1 minute on a hot plate.

Etching and Resist Removal

The wafer is now ready for etching. It is etched with a Ta-111 etchant for 8 seconds, then rinsed with DI water and dried with N_2. During the etching process, the metal is removed only from the areas not covered by the resist, while the regions protected by the resist remain intact (in Fig. 3.4(e)). This process defines the ground plane of the structure.

The remaining resist is removed by soaking the wafer in acetone for about 2 hours, followed by rinsing with IPA and drying with N_2 (in Fig. 3.4(f)). Finally, the circuit layout is complete and ready for the next steps, such as Josephson junction fabrication and airbridges.

CHAPTER 4

Airbridges

This section will address the fabrication process of airbridges and different methods used in the literature for airbridge fabrication. Additionally, the yield of the fabricated devices in this thesis will be discussed later in this section. Moreover, a full recipe for airbridges is given in the Appendix. All fabrication processes described in this thesis are conducted at the QNZT at the University of Innsbruck.

Airbridges have been fabricated using various methods for decades, including photolithography and electron beam lithography (EBL), specifically grayscale EBL (G-EBL). In general, airbridges can be fabricated from different materials and the main considerations are mechanical stability, good electrical contact and low-loss characteristics.

4.1 Overview of Airbridge Fabrication Methods

In this section, we provide an overview of airbridge-related literature, highlighting key properties and specialized fabrication techniques. For a more detailed explanation of each process, the original papers are recommended, as referenced in Table 4.1. The table summarizes the fabrication details of each method. The second column lists the lithography techniques used, followed by the number of lithography steps required, where using fewer steps is generally more favorable. The fourth column describes the deposition techniques used for the airbridge layer, specifying the materials, whether a milling step is included and the thickness of the deposited layer. The "Temperature" column indicates the highest temperature involved during fabrication, where lower values are preferable. Finally, the table includes the maximum achieved airbridge length and the corresponding yield(if reported).

Author	Lithography Type	Lithography Steps	Material (Thickness of the metal film)	Temperature (°C)	Length (µm)
Abuwasib et al. [28]	Photolithography	Three-step	Al,no argon mill, 2µm	250	30–40
Janzen et al. [1]	G-EBL	Single-step lit., selective reflow	Al,argon mill, 450nm	180	36
Sun et al. [27]	Gray-photolithography	Single-step, no reflow	Al,argon mill, 500nm	95	200
Chen et al. [29]	Photolithography	Two-step, reflow	Al,argon mill, 300nm	150	40
Girgis et al. [33]	G-EBL	Single-step, no reflow	Au,no mill, 200–350nm	200	12
Jin et al. [30]	EBL	Single-step, no reflow	Au,no mill, 110–130nm	150	5
Tao et al. [31]	Photolithography	Two-step, no reflow	Nb,argon mill, 700nm	200	70
Stavenga et al. [34]	G-EBL	Two-step, reflow	NbTiN,no mill, 200nm	150	–
Bu et al. [35]	Photolithography	Two-step, reflow	Ta,argon mill, 400nm	140	60
Bolgar et al. [32]	Photolithography	Two-step, no reflow	Al,argon mill, 420/840nm	115	500(75%)

Tab. 4.1 Airbridge Fabrication Methods from Selected Studies.

4.1.1 Al Airbridges

One of the widest airbridges was fabricated by Abuwasib et al. [28], with widths of 300–500 μm and heights of 8.5 and 15 μm. This method avoids local ground equalization via wirebonds, but comes at the cost of introducing large shunt capacitance and increased reflection at the bridge connection. The fabrication process began with spinning a layer of PMGI SF15 photoresist, which defines the height of the airbridge, followed by a layer of S1813 as the imaging layer. The stacked photoresist was then exposed by using a mask aligner with broadband UV light. After development, a positive profile was formed to serve as the support layer of the bridge. Next, the resist stack was soft-baked before development at 160°C, a relatively low temperature was chosen to produce an undercut profile. This temperature also increases the solubility of the resist. The imaging layer was then removed by a second UV exposure (8 s) and a short development step, since the MF319 developer can attack the Al CPW layer. To achieve the desired arched shape of the bridge profile, the photoresist mask was reflowed by heating it to 250°C, which softens the resist and smooths its surface. For a clean lift-off process, the lift-off layer must be at least 2 μm thicker than the support layer, as a 2 μm-thick Al layer will later be used for the airbridges. For the 8.5 μm and 15 μm airbridges, at least 10.5 μm and 17 μm of negative-tone photoresist (SU-8 2035) were used. The unexposed resist served as the sacrificial layer for lift-off. Afterwards, a 2 μm Al layer was evaporated using an e-beam evaporation system at a 0° angle. Finally, the sample was subjected to lift-off to remove the unwanted resist and excess Al. At this stage, rinsing with IPA was recommended over DI water due to its lower surface tension, which helps to avoid bridge collapse during drying.

Another method of fabricating airbridges involves etching Al strips instead of using the standard lift-off process [29]. First, a 3 μm-thick layer of positive-tone photoresist (Megaposit SPR-220-3) was spin-coated, defining the height of the airbridge. The resist was then exposed to define the boundaries of the airbridges and reflowed at 140°C to create the arc shape of the mask. This was followed by aluminum deposition using e-beam evaporation, in which a 300 nm-thick Al layer was deposited after an argon ion milling step to remove the native aluminum oxide layer. A second layer of photoresist was coated as a protective layer for the wet etching process. The unexposed area of this second resist layer defines the width of the airbridge, while excess aluminum

was etched away using Transene Aluminum Etchant Type A for 5 minutes. At this stage, the ground plane around the bridge pads was not protected by photoresist. After etching, all resist layers were stripped to release the airbridges. Since the argon ion milling leaves significant resist residue, an O_2 plasma cleaning at 150°C was performed before stripping the resist. Using this process, airbridges up to 50 μm were successfully fabricated. Additionally, the authors tested coating a two-layer resist stack on the fabricated airbridges to fabricate Josephson junctions. Air bridges with lengths up to 40 μm were reported to withstand this process without damage. However, it was also reported that airbridges fabricated by this method did not survive sonication.

The mechanical strength of airbridges can also be improved by modifying their geometry. Bolgar et al. [32] reported achieving a 100% yield for airbridges up to 170 μm in length. This was accomplished by introducing a stiffener, an elevated section running along the center of the airbridge. Instead of using a conventional flat strip, this design added structural support, improving the mechanical stability of longer airbridges. This method does not require grayscale lithography or resist reflow. In crush tests, airbridges with stiffeners were found to be durable to nitrogen (N_2) blow pressures up to 4.0 atm in impulse mode, which is significantly higher than what airbridges without stiffeners can withstand.

4.1.2 Other materials

Niobium airbridge

Airbridges can also be fabricated using different materials. Nb is a promising option due to its higher critical temperature, larger superconducting gap, lower thermal quasiparticle loss, high mechanical stability and resistance to aggressive cleaning processes such as HF [51]. Because of these advantages, Nb is considered a suitable material for airbridges. However, the fabrication process differs slightly due to the higher deposition temperature of Nb and the need to avoid resist residues. As reported by Tao et al. [31], aluminum (Al) was used as the sacrificial layer in this process. In the fabrication steps for Nb airbridges, a bilayer photoresist stack of LOR 5B and S1813 was coated onto a wafer that had been wet-etched using buffered oxide etch (BOE). Standard photolithography was used to define the bridge pattern. A 2 μm undercut was targeted to ensure a clean lift-off. For improved mechanical strength, a 300 nm sacrificial Al layer was deposited using an e-beam evaporator at three different angles: 45°, 90° and 135°. Lift-off was performed in an NMP bath at 80°C. Next, Ar ion milling was used to improve ohmic contact, followed by the deposition of a 700 nm Nb layer using magnetron sputtering. Photoresist was then coated and patterned again to serve as an etch mask. The masked wafer was etched using a CF_4 plasma and the photoresist was removed using NMP. The sacrificial Al layer was etched away to release the Nb airbridge. Using this process, they reported achieving losses per bridge of the order of 10^{-9} at the single-photon level [31].

Tantalum airbridge

Ta is also widely used in superconducting circuits due to its high coherence times and resistance to alkali and acids. To take advantage of these properties, stable Ta airbridges for high-performance superconducting circuits were realized by Bu et al. [35]. Similarly to the fabrication process of the Nb airbridge, an Al sacrificial layer was used, but in a much thinner

form, approximately 25 nm. After defining the mask and performing a reflow step to achieve a smooth profile, another resist stack was coated to define the bridge structure. The Al layer was then etched away and a 400 nm Ta layer was deposited using magnetron sputtering after Ar ion milling to improve contact quality. Before the final lift-off, a Transene Aluminum Etchant Type A bath was used to remove any remaining Al residue and release the airbridges. Like Nb, Ta airbridges have been reported to exhibit loss per bridge on the order of 10^{-9} at the single-photon level, indicating that both materials offer a lower loss than Al airbridges.

4.2 Fundementals of Nanofabrication

Nanofabrication is a widely used technique for creating micro- and nanoscale structures across various fields of research. In this section, we introduce the fundamental concepts of micro- and nanofabrication methods.

4.2.1 Grayscale Electron Beam Lithography

Lithography is the process of writing two-dimensional or three-dimensional patterns by energy deposition using photon or electron sources on light- or electron-sensitive materials. Light-based lithography is called photolithography, while electron-based lithography is referred to as electron beam lithography (EBL). There are also other types of lithography, such as extreme ultraviolet (EUV) lithography, focused ion beam lithography and neutral atomic beam lithography. For more details, the reader is referred to Refs. [52, 53]. Current lithography techniques enable patterning at scales ranging from nanometers to micrometers. The process begins with imprinting a layout on the surface, typically using a resist and chemically modifying the structure.

Resists are typically organic compound-based materials that are used to create masks through energy deposition by photons or electrons. Resists are categorized as either positive-tone or negative-tone. In positive-tone resists, exposure modifies the chemical composition of the resist and makes it soluble in the developer solution [54]. After development, the areas exposed by photons or electrons are removed and the remaining resist defines the final pattern. In negative-tone resists, the exposed regions will be polymerized, making them more difficult to remove, while the unexposed regions are dissolved throughout the development process. Either type is useful in various fabrication techniques, but all the fabrication processes in this thesis are conducted using positive-tone resists.

Electron Beam Lithography (EBL) systems have been in use since the 1960s and are considered one of the milestones in micro- and nano-fabrication. One of the advantages of EBL is that, unlike photolithography, it is not limited significantly by diffraction effects [55]. However, EBL is limited by proximity effects due to backscattered electrons [56], especially in systems operating at lower acceleration voltages, which limits the resolution of the patterns. Current algorithms for proximity correction can effectively suppress this effect, as we will discuss in more detail later. We use EBL to achieve smaller and more precise features. Additionally, the system is limited by the writing field and the resolution of the EBL system. In particular, the resolution is limited by Coulomb interactions between electrons and resist molecules, secondary electrons, and electrons scattered by the substrate. At the QNZT, we use a 30kV Raith e-line plus lithography system.

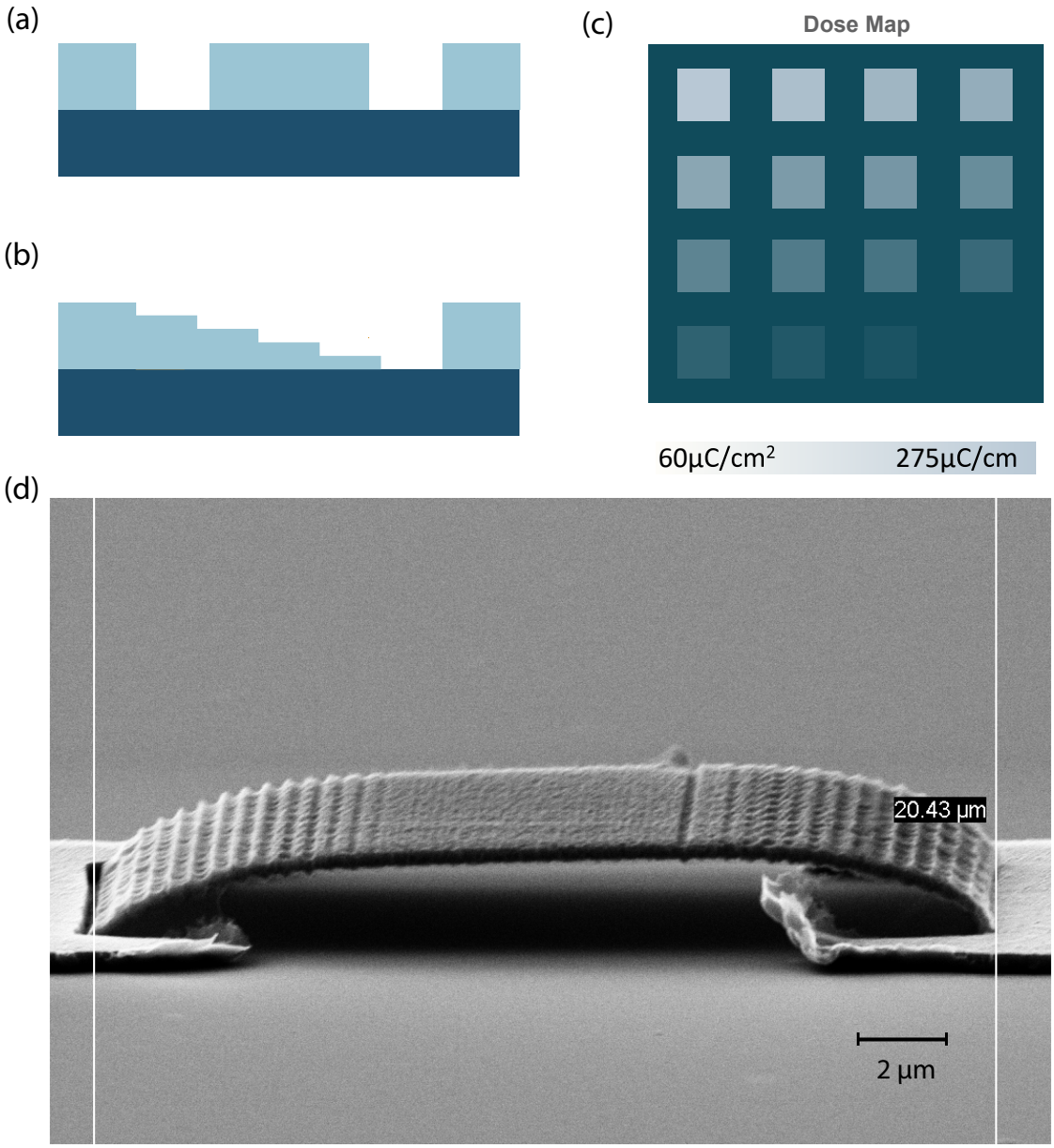

Fig. 4.1 (a)(b) Illustrations of binary lithography and grayscale lithography results after development. (c) Representative dose map for grayscale lithography, higher dose is responsible for lower height after development. (d) The first airbridge without using the proximity effect correction and reflow of the sacrificial resist mask.

Having a three-dimensional structure in nano- and micro-fabrication is essential for state-of-the-art optical and electromechanical devices such as microlenses, MEMS and airbridges [1, 57, 58]. 3D maskless lithography has paved the way for higher-performance, higher-yield devices with fewer processing steps.

The technique known as grayscale lithography enables the creation of smooth 3D shapes for

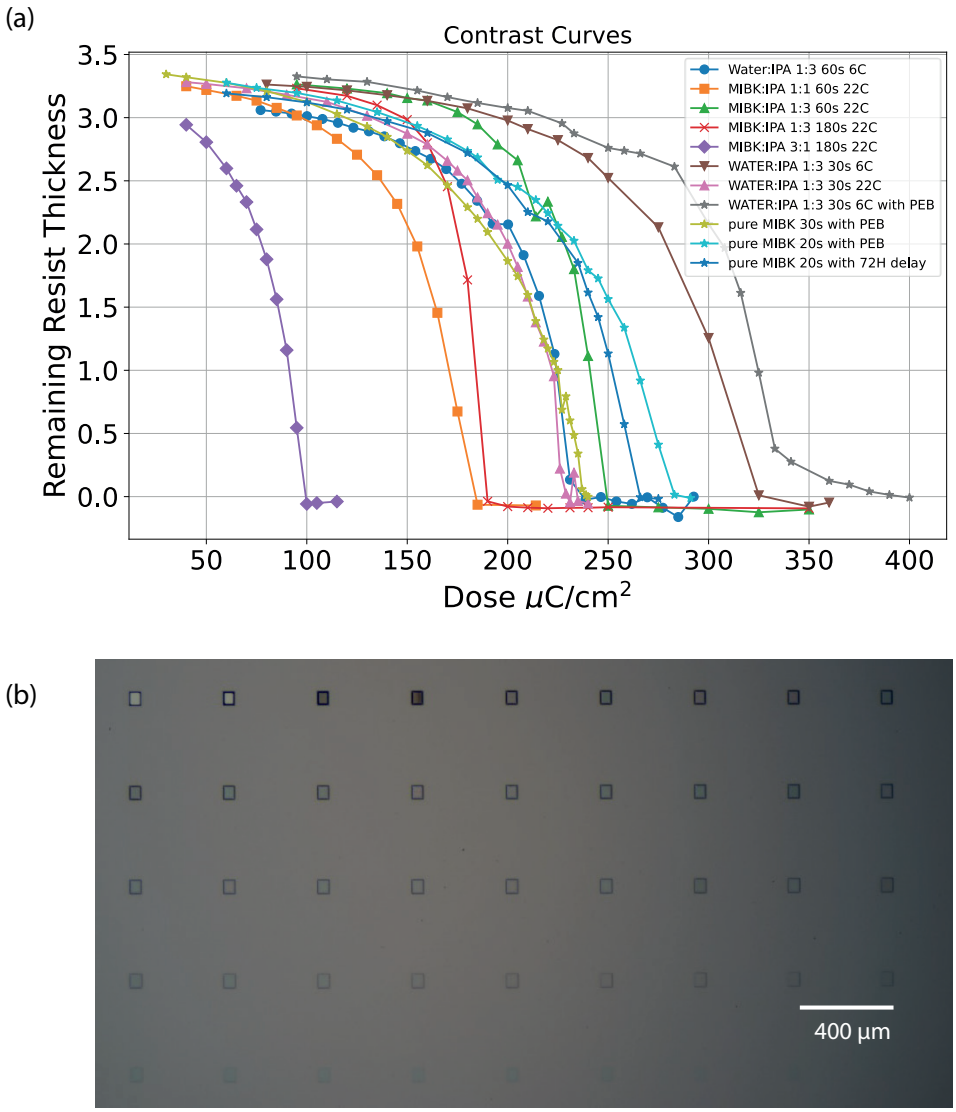

Fig. 4.2 (a) Contrast curves for different development conditions. (b) The dose map used in design was generated from 50×60 rectangular area exposed with different EBL doses.

structures such as photonic circuit mirrors by varying the dose across the mask using either photolithography or electron-beam lithography (EBL). In particular, grayscale EBL aims to create masks with varying heights after development, as illustrated in Fig. 4.1(b). This process is usually followed by reflowing the exposed resist — in other words, melting it at a specific temperature — to achieve a smooth 3D surface. In conventional lithography, which is essentially a binary process (developed to the bottom or unexposed) as illustrated in Fig .4.1(a), a single dose is used to produce a sharp mask after development. Airbridges can be fabricated using either grayscale lithography or binary lithography. Binary lithography often exhibits lower strength and yield due to its rigid structure, or it requires a high temperature to reflow the resist

in order to achieve an arched shape. However, the higher temperatures required for reflowing can adversely affect the performance of superconducting circuits by altering the resistance of Josephson junctions [34].

The variation in height is controlled by both the exposure dose, which refers to the number of electrons per unit area and the development parameters, which include development time, temperature, and the type of developer used. In EBL, the system can be programmed to expose columns with varying exposure times, which changes the exposure dose. Before creating the final layout, one needs to know which dose corresponds to which height, so a dose test is first performed by exposing, for example, 50×50 µm boxes with different doses as illustrated in Fig 4.1(c). Since all of the boxes are on the same wafer, they are developed under identical conditions, so each box corresponds to a different depth in the resist as shown in Fig.4.2(b). After development, a profilometer or AFM can be used to measure the resulting depths of each box, and a contrast curve can be obtained by plotting the remaining resist thickness versus the corresponding dose, as shown in Fig. 4.2(a).

In conclusion from the dose tests, the cold development method using a Water:IPA mixture of 1:3, which is available in the QNZT, is very precise for binary lithography because cooling slows down the development reaction. However, it is not commonly used in grayscale lithography. Although this method resulted in relatively low contrast in our process, the resulting mask was not stable and showed slight variations across different fabrication runs and the reason for this remains unknown. Here, contrast refers to how sharply the resist changes from unexposed to fully developed within the linear region of the contrast curve during processing [30]. In addition, various developer solutions with different development times were tested, as shown in Fig. 4.2(a) and Table 4.2. For example, mixtures of MIBK and IPA with different ratios and development durations were investigated. It is clear that longer development times increase the contrast and decrease the dose at which the resist is fully developed. In addition to achieving low contrast, increasing the range between the highest and lowest doses also provides higher precision. This change in range can be observed for 60 s and 180 s development in MIBK:IPA 1:3; longer development times result in a decrease of the peak dose by more than $50\,\mu C/cm^2$. Moreover, development in H_2O:IPA 1:3 mixture for 30 s was tested at both cold and room temperatures. It is clearly seen that colder development decreases the contrast and provides good results for grayscale EBL applications. Since there was only one cold developer available in the QNZT, we could not test cold development for the other developer solutions. However, the best result with the highest stability was found to be using pure MIBK at room temperature, which was reported to be highly compatible with grayscale lithography process [2].

These dose tests were then used to design the layout of the 3D structures, providing complete control over the arrangement in the X, Y and Z directions. Subsequently, an arched shape can be created by employing resist with varying heights, resulting in step- or ladder-like structures as can be seen in Fig 4.1(b,d). Achieving a low-contrast dose curve is crucial because it minimizes the impact of proximity effects and the resolution limitations inherent in EBL. Furthermore, methods such as proximity correction, post-exposure bake and delayed development are employed to improve precision and yield. These methods will be discussed in more detail in the following sections.

4.2.2 Proximity Effect Correction

The precision of EBL has been mainly limited by the proximity effect, which can generally be excited by back or forward-scattered electrons [59] and beam blur. These limitations prevent one to obtain the mask intended by design after the exposure. On the other hand, these proximity effects can be corrected by the use of a commercial software such as BEAMER [60].

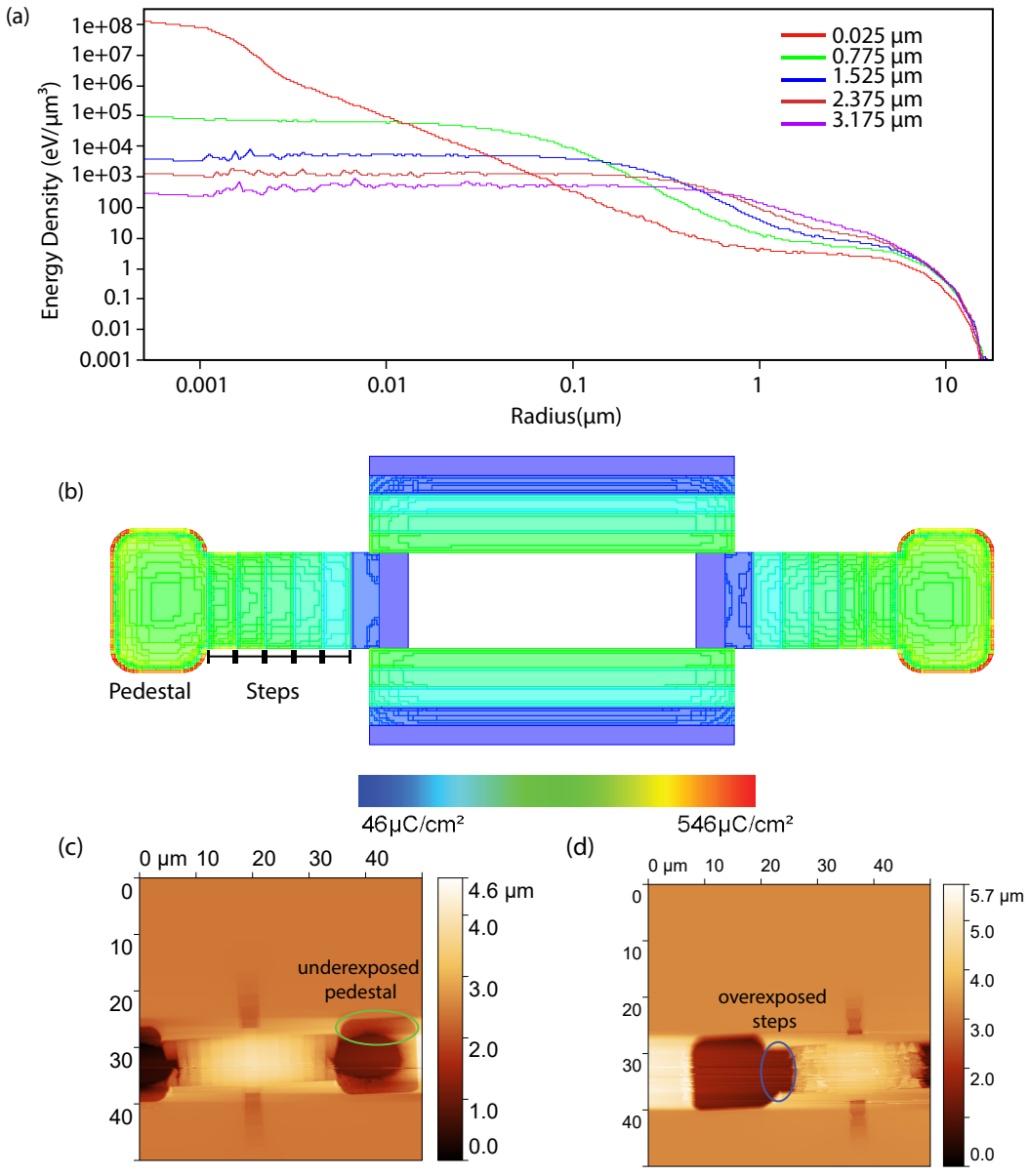

Fig. 4.3 (a) PSF function of 30keV e-beam into ARP 672-11 for different depths in the resist as a function of radius that affected area from the e-beam. (b) Proximity effect corrected airbridge design. (c, d) Atomic Force Microscopy images without and with proximity effect correction, respectively. Without correction, pedestals are poorly exposed with residual resist (green circle in c) and the first two steps are overexposed unintentionally (blue circle in d).

As electrons travel through the material stack, some are reflected from the substrate back into the resist—a process known as backscattering of the electron beam—which causes energy deposition at distances farther from the original beam position, depending on the scattering angle. Depending on the scenario, the backscattered energy distribution as a function of distance can be modeled using one or more Gaussian functions. The shape of this distribution is significantly influenced by the electron beam energy and the properties of the material stack, particularly the substrate. At higher energies, such as 100 kV, long-range backscattering becomes simpler and is often well described by a single Gaussian function.

On the other hand, the electron beam is also affected by elastic collisions with resist molecules, known as forward scattering. This effect becomes more significant as the resist thickness increases and the kinetic energy of the electrons decreases. Since we use more than 3 μm of resist for the airbridge mask and a 30 keV electron beam lithography system, forward scattering is particularly important in our process. The energy of the electrons in the deeper regions of the resist is significantly reduced, even directly at the beam position, as shown in Fig. 4.3(a), and the area of impact becomes wider around the beam position (as indicated by the radius). As a result, when the electron beam exposes one spot, it also partially affects nearby spots, especially in the deeper parts of the resist. This process increases the applied electron dose. This effect is considerably compensated by the proximity effect correction, but it is still present.

The Point Spread Function (PSF), which shows how energy is scattered as a function of distance r from a single point of exposure, is often used to explain the proximity effect. This function is used to describe how energy is propagated. PSF may be derived by Monte Carlo (MC) simulations performed by the TRACER software or through experimental exposure and analysis of test patterns. For the purpose of incorporating the PSF into the correction process, the BEAMER is able to collaborate directly with the TRACER.

Moreover, binary PEC is unlikely to be sufficient for 3D layouts; thus, simulations are performed for different resist stack heights, requiring multiple PSFs due to the thicker resist used in 3D masks. The distributions of energy density in the PMMA resist stack at a single point are shown in Fig. 4.3(a). These distributions were simulated using the TRACER software to determine the corrected dose in the layout. This was done using the BEAMER software, which divides large areas into small trapezoids and calculates the effective dose needed to achieve the desired geometry. The revised air-bridge design in Fig. 4.3(b) shows that achieving the desired shape for the sacrificial mask requires a non-uniform dose distribution. Specifically, the edges of the pedestals need a higher dose to produce steep edges, while the dose should decrease toward the center of the exposed areas to minimize overexposure.

Steep edges are essential for facilitating lift-off, since the unexposed resist at the edges (as seen in the green circle in Fig. 4.3(c)) will also be covered during metal deposition. The goal of applying PEC is to make these edges as close to 90° as possible, as can be seen in Fig. 4.3(d), so that metal deposition is minimized at the edges during the evaporation process. The much thinner Al at the edges can then be easily etched away, breaking the connection between the Al metal on top of the sacrificial mask and the fully exposed bottom layer, which increases the yield of the air bridges. Since the 3D PEC still operates with some imperfections, it overdoses the first two levels (highlighted by the blue circle in Fig. 4.3(d)), resulting in airbridges that are about 10 μm shorter than designed. Therefore, the airbridges should always be designed slightly

longer than required. Note that the AFM images of the airbridge masks (in Fig 4.3(c,d)) are not from the design shown in Fig. 4.3(b), since the AFM can scan only up to 50×50 μm in a single scan, while the airbridges used are much larger. Therefore, the straight part of the airbridges was minimized in order to fit within the AFM scan area.

4.2.3 Development

In this section, we will discuss in more detail the special development techniques used in this thesis, which are called delayed development and post-exposure bake (PEB). In most binary lithography processes, high contrast is desirable—unlike in grayscale EBL (g-EBL), where flatter dose-response curves are preferred to better control resist height and minimize errors in both exposure and development. To achieve this, different development temperatures, developers, and durations were tested in this thesis, as mentioned in the previous section and shown in Table 4.2.

Development time and exposure dose work together to produce accurate and reliable masks. Since EBL is also limited by the minimum usable dose, which is determined by the shortest exposure time of the system, selecting appropriate development parameters is essential for obtaining a low-contrast dose map. Increasing the electron beam dose generally shortens the required development time. However, establishing a repeatable process is essential before finalizing the development time, as the minimum development time is constrained by reproducibility.

Developer	Development time	Temperature	PEB or delay	Contrast
Water:IPA 1:3	60s	6°C	X	4.91
MIBK:IPA 1:1	60s	22°C	X	4.72
MIBK:IPA 1:3	60s	22°C	X	7.3
MIBK:IPA 1:3	180s	22°C	X	12.6
MIBK:IPA 3:1	180s	22°C	X	4.46
Water:IPA 1:3	30s	6°C	X	5.22
Water:IPA 1:3	30s	22°C	X	5.5
Pure MIBK	30s	22°C	Hot plate for 10min at 60°C	3.78
Pure MIBK	20s	22°C	Hot plate for 10min at 60°C	4.11
Pure MIBK	20s	22°C	72h delay	5.03
Water:IPA 1:3	30s	6°C	Hot plate for 10min at 60°C	6.57

Tab. 4.2 The table corresponds to different conditions of development.

An alternative approach to obtaining a wider dose map involves delaying the development process after exposure under room temperature conditions, as shown by Mortelsman et.al. [2]. In summary, they reported a clear relationship between delay time and the resulting resist depth after development, as shown on the left in Fig. 4.4. They simply exposed the resist to various doses ranging from 40 μC/cm^2 to 260 μC/cm^2, kept it at room temperature for different durations, developed the samples identically, and measured the resulting resist depth. Regions exposed to higher doses (260 $\mu C/cm^2$) are more affected by the delay time, while regions near the surface, which correspond to lower doses (40 $\mu C/cm^2$), are less affected. This helps achieve a wider dose map, which means that increasing the dose range between unexposed and fully exposed areas results in higher precision. In the most affected regions, it has been reported that

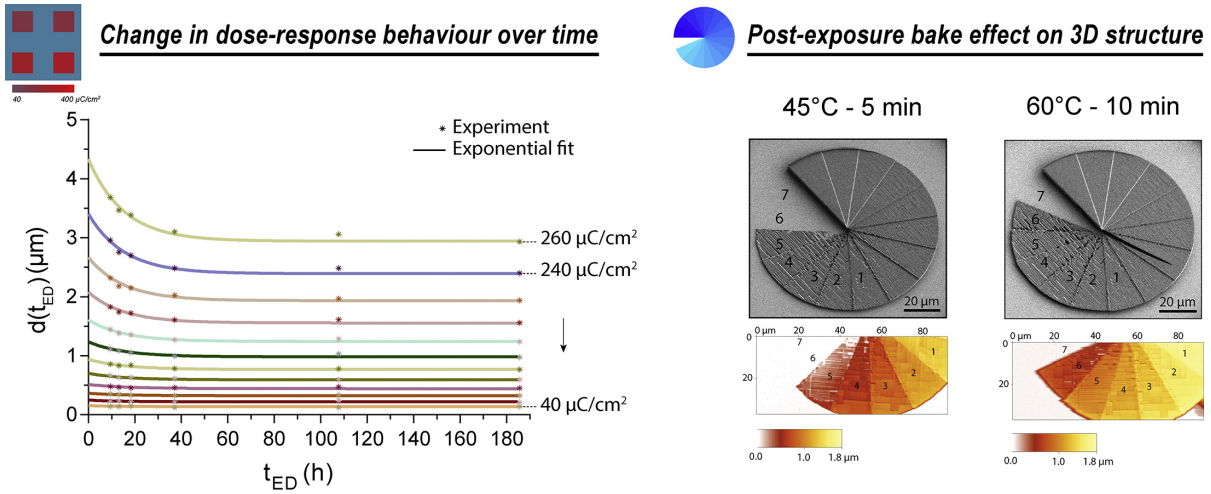

Fig. 4.4 The left graph shows the resist depth after development as a function of the delay time between exposure and development. The right graph shows the effect of post-exposure bake. The figure is taken from[2].

the resist depth decreases by approximately 1 μm at a dose of 260 μC/cm^2, while at the lowest dose of 40 μC/cm^2, there is almost no observable difference in the resulting resist depth after 180 hours [2]. The observed behavior follows an exponential decay, which can be modeled by an exponential relaxation function

$$d(t_{ED}) = (d_0 - d_{ss})e^{-\frac{t_{ED}-t_0}{\tau}} + d_{ss}, \tag{4.1}$$

where $d(t_{ED})$ is the amount of resist removed after development at a given delay time, τ is the time constant, and $d_0$and d_{ss} are extracted from the exponential fit. To ensure fabrication stability, the flat region in the curve is used as a reference in this thesis, since the resists are identical to those in the reference work [2]. For our process, approximately 72 hours is sufficient for the same E-beam resist (ARP-672.11). Immediate development after exposure is challenging, as some exposure processes can take up to six hours. Consequently, the first and last exposed areas are affected differently due to the extended time gap. During recipe development, there were also issues with uniformity across the wafer: some masks appeared overexposed, while others appeared underexposed. At first, we suspected a focusing issue with the E-beam and began using the autofocus function on the Raith E-line Plus system, but this did not resolve the problem. The effect of the delay between exposure and development provides a plausible explanation for the observed instability in long exposure sessions. Implementing a 72-hour delay effectively resolved both the non-uniform development across the wafer and the overexposure problem.

The fundamental process relates to the relaxation of broken PMMA chains. The electron beam breaks chemical bonds, increasing solubility. Over time, at room temperature, these broken connections experience relaxation or partial recombination, therefore reducing the solubility of previously exposed areas. This results in an increase in the maximum dose threshold before full

development occurs. Similarly, heating can be used to accelerate this relaxation process—using a hot plate or oven—instead of relying on passive room-temperature aging, as shown on the right in Fig. 4.4, which refers to post-exposure bake. In that experiment, they sliced two cir-

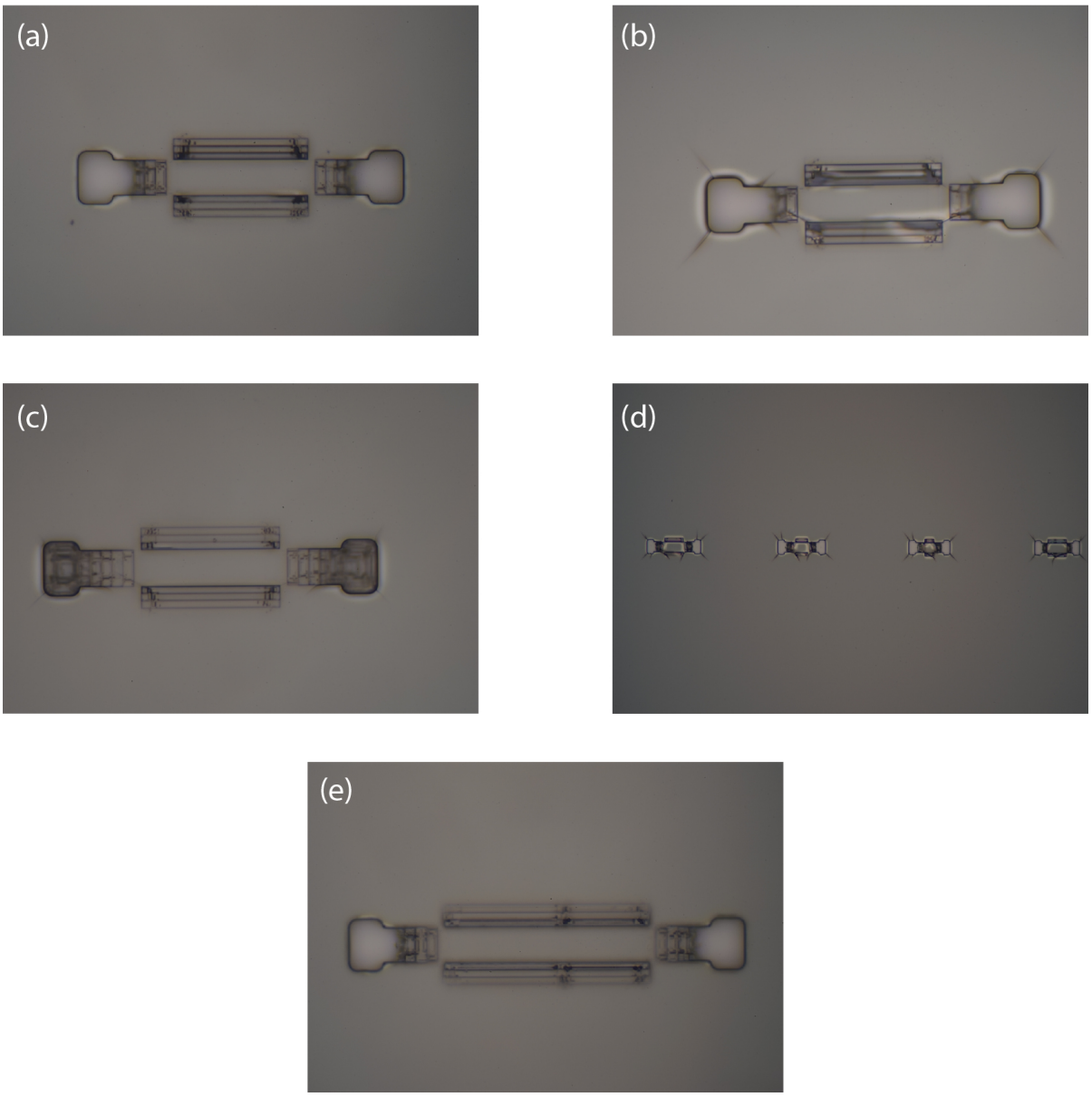

Fig. 4.5 Resist masks after development under various post-exposure conditions: (a) 45°C for 20 minutes on a hot plate; (b) 55°C for 10 minutes on a hot plate; (c) 60°C for 2 hours in an oven; (d) 70°C for 10 minutes on a hot plate; and (e) development delayed by 72 hours after exposure.

cular structures like pie charts, exposing each segment (from 1 to 7) to a different dose. Then the two samples were baked under different conditions: one at 45,° C for 5 minutes and the other at 60,° C for 10 minutes, then both were developed under identical conditions. The results show that the sample baked at the higher temperature still has remaining resist in segment 6, while the sample baked at the lower temperature is fully developed at the same exposure dose.

The delayed development method worked very well for the masks shown in Fig.4.5(e), with the obvious drawback that it required a waiting time of 72 hours. Thermal treatment was explored to reduce processing time. Increasing the temperature enhances tolerance to higher doses and broadens the usable dose range, similar to the effect of delaying development at room temperature [2]. However, this approach is limited by the thermal stress applied to the resist.

A treatment at 70°C on a hot plate for 10 minutes increases the dose threshold significantly (up to 420 μC/cm^2), but when applied to smaller features such as airbridges, it causes cracks in the resist, as shown in Fig. 4.5(d) and also observed in (b) and (c). The oven provided a more uniform temperature distribution than hot plate. However, the treatment at 60°C for 2 hours improved the dose threshold similarly with the 70°C on a hot plate, although cracks were still observed. The best overall condition was found to be baking at 45°C for 20 minutes on the hot plate. This approach extended the dose range without introducing cracks, as shown in Fig 4.5(a). With this method, the fabrication process became more reliable and significantly faster.

4.2.4 Metal Deposition

The circuit layers require metal thin film deposition, which is achieved through either sputtering or evaporation, both of which are physical vapor deposition (PVD) techniques. Most PVD processes involve the synthesis of vapor from the source, targeting the substrate, and finally, condensation onto the substrate [61]. The process is carried out in a vacuum chamber to avoid impurities in the thin film.

The *Plassys MEB550S* e-beam evaporation device is often used in the QNZT for the deposition of metallic thin films. A high energy electron beam focuses on the source material (Al, Ti, Nb) and causes the evaporation of its atoms. These evaporated atoms then hit the colder sample holder and condense onto the substrate. This process is conducted under high vacuum conditions ($< 10^{-6}$ mBar), which typically requires at least one hour of pumping to achieve this pressure before starting the evaporation.

The evaporation rate is measured using a quartz crystal oscillator. The rate is also significantly influenced by the material's boiling point and can be regulated by modifying the power of the electron beam. The shutter between the source and the substrate stays closed until a consistent evaporation rate is achieved. E-beam evaporation provides both a high deposition rate (50–500 nm/min) and high-quality films.

4.3 Airbridge Fabrication

Many fabrication techniques have been developed to achieve airbridges with sufficient length and width using various materials. Specifically, airbridges are designed for superconducting circuits, including qubits and must be compatible with all aspects of these systems. For example, they must be fabricated at the lowest possible temperatures [34], since they are often added after all other layers of the superconducting circuit are complete. Different materials offer var-

ious advantages and disadvantages, such as mechanical durability, high coherence, low loss, or ease of fabrication. In this section, different fabrication methods will be discussed in more detail.

This thesis has devoted considerable attention to E-beam lithography using a notably thick single layer in grayscale lithography with low-acceleration voltage E-beam lithography (EBL), a practice that is uncommon in most grayscale lithography applications. To accomplish this, additional steps and adjustments are incorporated into the fabrication process, such as post-exposure bake, delayed development and proximity effect correction, as discussed in the previous section.

4.3.1 Sacrificial Layer of Airbridges

After fabricating all other layers on wafers, such as CPWs and Josephson junctions, we start fabricating the airbridge layer. Before the wafer is coated by E-beam resist for the airbridge mask, the wafer should be cleaned with hot acetone for 5 min at 50°C in an ultrasonic bath, then rinsed by Isopropanol Alcohol (IPA) and dried with nitrogen blow. Then, the wafer is mounted on the spinner and does not move while the spinner is running due to the vacuum being activated. In addition, cleaning the surface with a nitrogen gun is recommended after the vacuum is activated to avoid particles on the wafer, which can disturb the spinning procedure by altering the flow direction of the resist. Then, 2.5 ml PMMA resist "ARP 672.11" is dispensed onto the wafer by a pipette. At this point, it is essential to prevent the introduction of air bubbles from the pipette as these could negatively impact the coating. It is recommended to refrain from using the entire resist in the pipette to avoid the discharge of air onto the wafer.

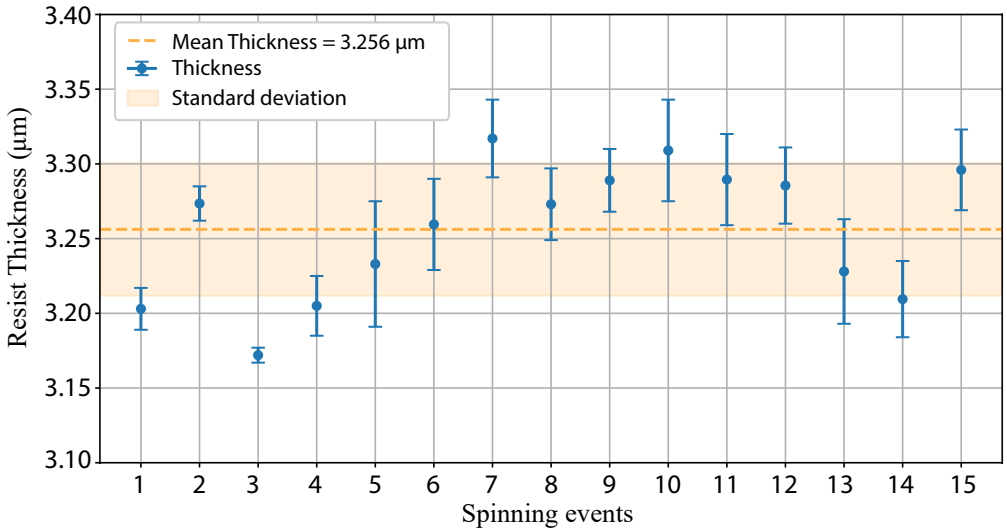

Fig. 4.6 Thickness measurements of the ARP 672.11 under identical conditions with error bars mean line and standart deviation.

The spinning process begins at 500 rpm for 5 seconds to approximately distribute the resist, facilitating the creation of a more uniform and reliable resist coating for particularly thick resists. Subsequently, the rotational velocity is elevated to 1250 rpm for a duration of 60 seconds with 100 rpm per second acceleration to achieve a film thickness of about 3.2 μm. The wafer is then

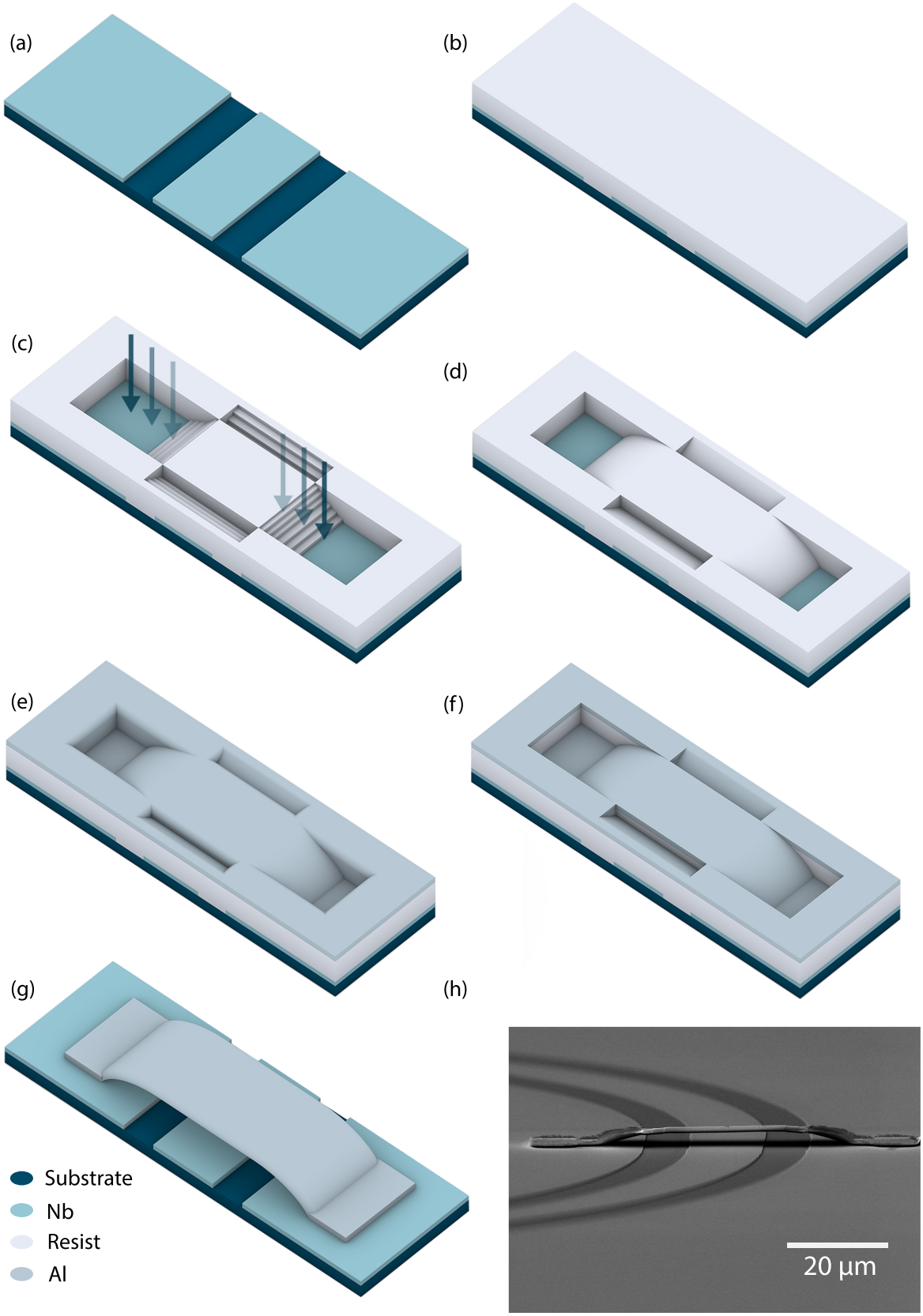

Fig. 4.7 Illustration of the fabrication process of Superconducting Airbridges. (a)Base layer of the circuit. (b) Resist coating. (c) Grayscale-electron beam lithography. (d) Reflow of the resist. (e) Al evaporation for the airbridge layer. (f) Wet etching for sidewalls. (g) Lift-off. (h) SEM image of the Airbridge on the CPW resonator.

placed on a hot plate for soft baking at 150°C for 3 minutes to eliminate the remaining solvent. Thickness control is essential prior to starting the exposure process, since variations in thickness may result in alterations to the dose necessary for grayscale lithography.

There are two common methods for measuring resist thickness, one can use a profilometer or an ellipsometer (Horiba SmartSE). Thickness can be measured right after coating using an ellipsometer with the Cauchy coefficients provided by the manufacturer [62], or it can be determined after exposing some layouts using a profilometer through a scan of the height difference between exposed and nonexposed areas.

To ensure a reliable film thickness, it is measured by the ellipsometer every time after the resist coating. As shown in Fig. 4.6, the mean thickness for 15 different spinning events at 1250 rpm is 3.256 μm, with a homogeneity of approximately 1.37%.

The resist coated wafer is mounted to the *E-line Plus* to expose the airbridge mask in a single lithographic step. In the current system, 30 keV acceleration voltage, 30μm aperture and high current mode are set. In addition, the auto focus mode is activated to stay on focus all over the wafer. The arch profile of the airbridge is created by varying the doses depending on the contrast curve (Pure MIBK for 20 s with PEB or delay) as seen in Fig. 4.2(a). The created mask is processed for proximity correction to have the final design of the bridge mask as seen in Fig. 4.3(b).

After exposure has been done, the wafer is rested for 72-hours at room temperature or baked on a hotplate at 45°C for 20-minutes. The wafer is developed in pure MIBK for 20 seconds at room temperature and then stopped in IPA and dried with a nitrogen blow.In the case of using the PEB method, it is recommended to allow the wafer to cool for a few minutes, as this may improve reproducibility. The revealed mask is checked under the optical microscope before continuing to the next step, as shown in Fig4.5(a). The fabricated mask has a well-defined stepped structure that resembles a ladder, with multiple levels formed due to dose variations during exposure. This profile clearly illustrates how different exposure doses create height differences in the resist, as indicated in Fig. 4.7(c). Then, the wafer is softbaked for reflowing the resist to smoothening the steps on a hot plate at 130°C for 1 minute as indicated in Fig. 4.7(d).

4.3.2 Metallic Layer of Airbridges

After a sacrificial layer of the airbridges is done, we start depositing the metal layer on top of the mask as indicated in Fig. 4.7(e). Aluminum is deposited using an e-beam evaporator. Prior to the evaporation of the metal, it is essential to etch away the native oxide layer on the surface to ensure a reliable galvanic connection between the airbridge pedestal and ground layer. This is achieved by accelerating argon ions with a potential and bombarding the substrate to mill the target, a process known as mechanical dry etching. During Ar^+ milling, the following parameters are used: beam voltage 400 V, accelerator voltage 80 V, beam current 22 mA and ion gun discharge 40 V.

Additionally, a Ti gettering step helps to improve the vacuum environment, as Ti is known to absorb oxygen, nitrogen, carbon dioxide, air, water vapor, hydrogen and methane [63]. A 24 nm Ti layer is evaporated at 0.2 nm/s while the sample is protected by the shutter, followed by a 450 nm Al layer evaporated at 1 nm/s, while the sample holder rotates at 5 rpm in a planetary

motion to improve film homogeneity.

After deposition of Al on the resist mask, the Al coats the entire surface unevenly depending on the angle of the surface. Since the sidewalls are nearly parallel to the evaporation direction, significantly less Al is deposited on the sidewalls, as indicated in Fig. 4.7(e) and (f), which are before and after the wet etching, respectively. During isotropic etching, which proceeds uniformly in all directions, the thinner sidewall regions of the Al structure are etched away much faster than the rest of the layer. As a result, the connection of the Al layers between the top of the resist and the pedestals is eventually severed. This disconnection enables easier lift-off and improves fabrication yield. An etching time of 3 minutes at 23°C in Transene Al Etchant Type A is typically sufficient for good lift-off results. The etching is stopped by placing the wafer in water, followed by drying with a nitrogen (N_2) gun. However, the actual etching time strongly depends on the oxide layer present on the Al surface, since the etchant first removes the oxide layer before attacking the underlying aluminum.

4.3.3 Lift-off the Excess Al Layer

As the last step, the fabricated device needs to be released by removing the resist without causing damage. The resist structure can be dissolved in specific chemicals such as acetone, NMP, or dedicated solutions. However, a method that allows the metal structure to remain on top of the substrate while removing the resist is called *lift-off*. After being diced into chip-sized pieces, the sample was left in *AR 600-71* at 70°C for at least 2 hours to perform the lift-off process. Finally, the fabrication process is finished and airbridges appeared as shown in Fig. 4.7(h).

Usually, a protective layer is coated on the wafer for the dicing step to protect the wafer from particles. However, the airbridges are not durable enough to withstand the spin coating process. In this case, the order of the fabrication steps is switched so that the Al layer is not lifted off and remains as a protective layer until the chip is diced into the desired shape.

4.4 Mechanical stability

The first consideration after fabricating airbridges is mechanical stability. Airbridges may be damaged during the fabrication process, whether from lift-off, sonication, or N_2 blow, they can be fully ripped off or collapsed. The ripped-off airbridges might redeposit on the circuit again and degrade the circuit, or even short the line. In addition, airbridges can collapse due to their own weight or external force, again resulting in circuit degradation or short circuit, as can be seen in Figure 4.10.

The yield of airbridges is quite important, as there can be several hundred airbridges on a single chip, and even a 99% yield can result in a few failed airbridges, potentially degrading or shorting the circuit. For different requirements, different sizes of airbridges have been developed, as shown in Figure 4.8(b).

Before deciding on the final length and width, yield tests were conducted. To estimate the approximate yield of the structures, airbridges with different lengths—25, 32, 45, 55, 65, 75 and

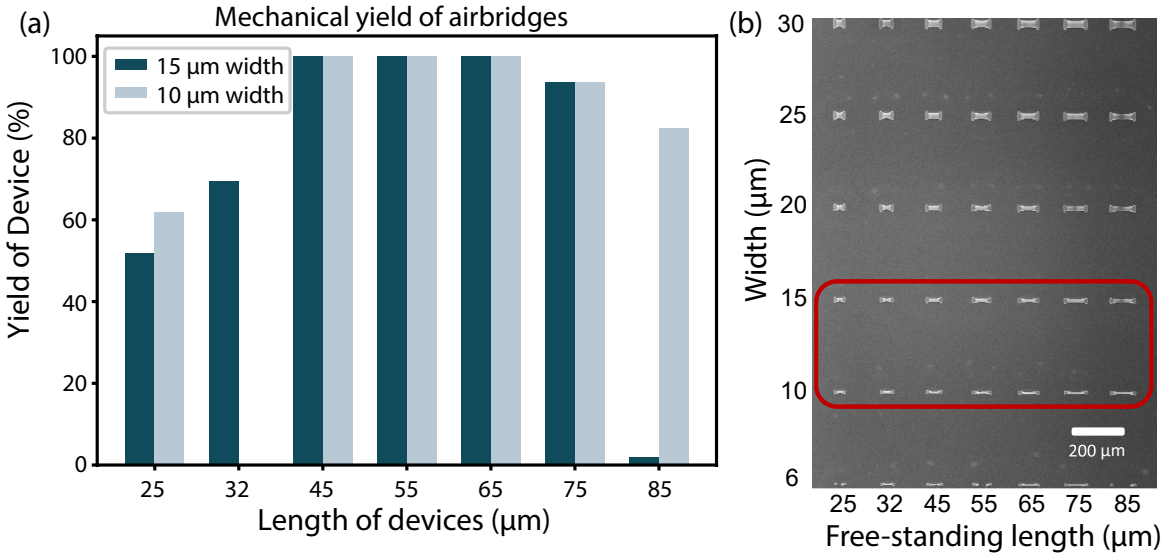

Fig. 4.8 (a) Mechanical yield of the fabricated airbridges for different lengths and widths. The different colors in the columns correspond to different widths of airbridges as highlighted at the top left of the graph. (b) SEM image of various airbridge designs, with free-standing lengths ranging from 25 to 85 μm and widths from 5 to 30 μm. The red square highlights the airbridges whose yield data are presented in (a).

86 μm—and widths of 10 and 15 μm were fabricated on the same wafer. For each design, 108 airbridges were fabricated and inspected using SEM. Finally, the airbridges that remained standing after fabrication are counted to determine the approximate yield, as shown in Fig. 4.8(a). However, an airbridge is counted as successful only if it stands alone with any sidewalls or residual metal.

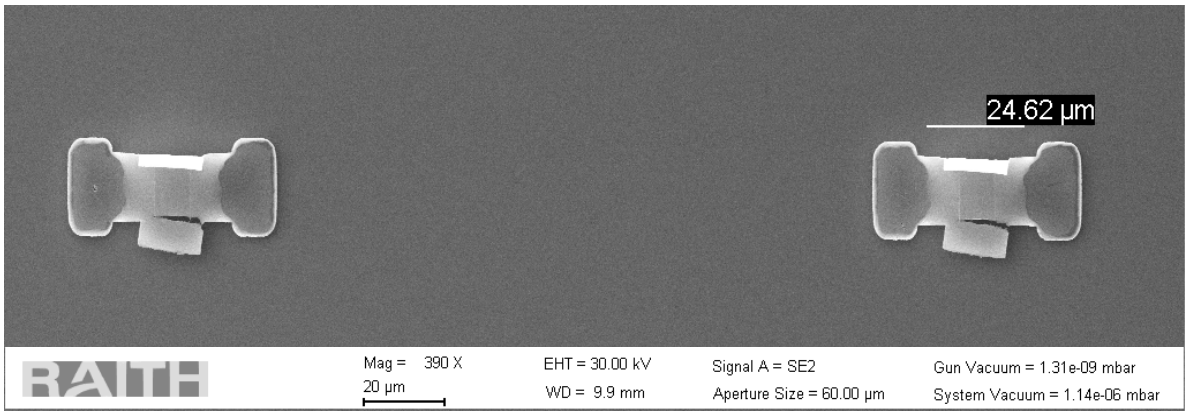

Fig. 4.9 The shortest airbridges often exhibit residual aluminum on the sides, which is considered a failure in the yield test.

The shortest airbridges, 25 and 32 μm, show very low yield even though they are all standing. This is because the sidewalls cannot be fully disconnected during the etching step, and the

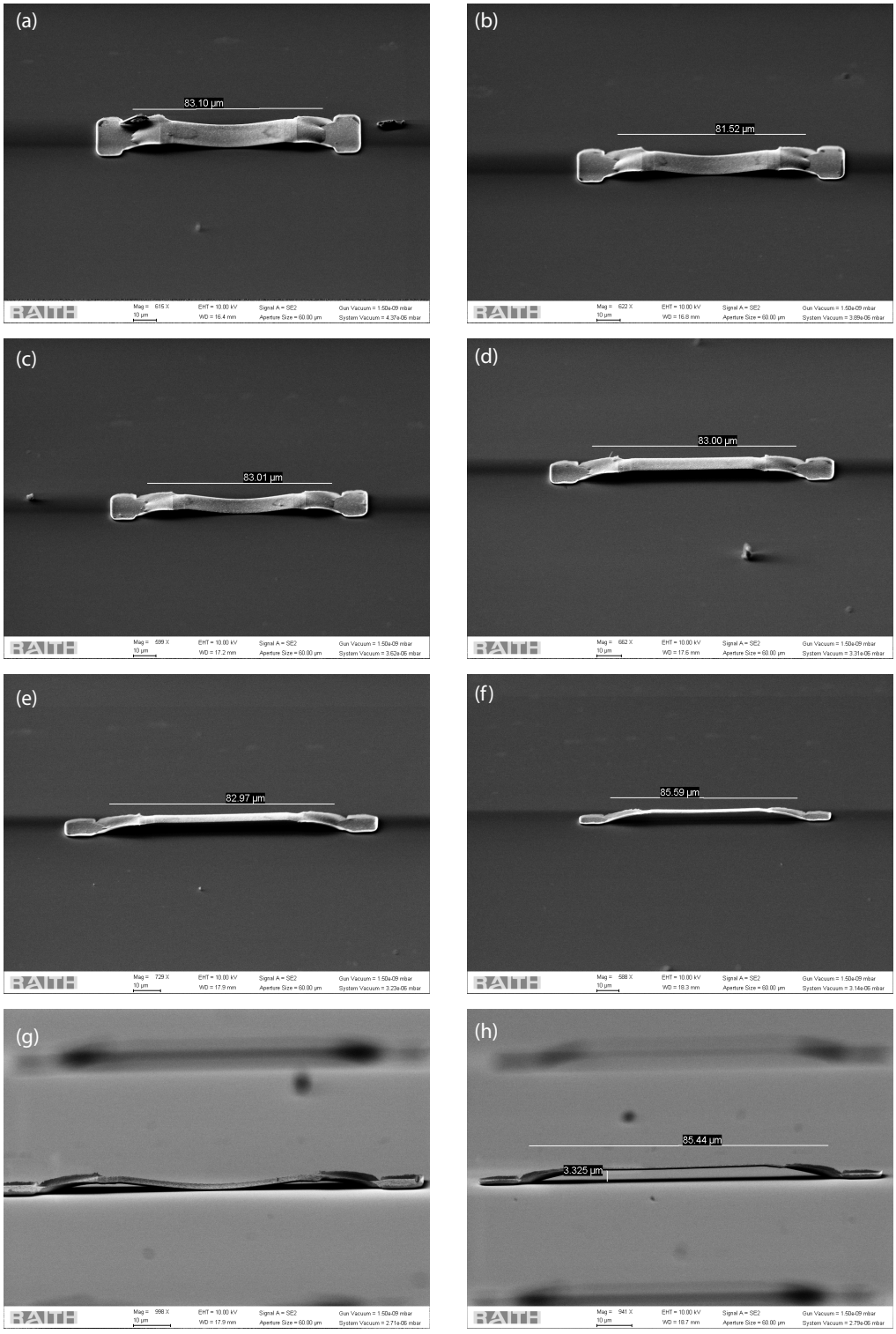

Fig. 4.10 Image of 85 μm length airbridges with different widths. From (a) to (f), the widths are 30, 25, 20, 15, 10 and 6 μm, respectively. (g–h) show the side profiles of the 20 μm and 10 μm wide airbridges.

remaining metal can be redeposited onto the circuit, as shown in Figure 4.9. Therefore, they are counted as failed. This problem could potentially be mitigated by extending the aluminum etching time.

For longer bridges—45, 55 and 65 μm—the yield is perfect within the same fabrication run. The 65 μm length and 10 μm width are later chosen for the Nb resonator on the sapphire substrate, as can be seen in Fig. 4.7(h). However, when the size increases to 75 and 85 μm, the yield decreases. This is because the weight of the aluminum strip increases and the structure may become unable to support its own weight, as shown in Fig. 4.10(a–c).

In contrast to most other works, sonication is not destructive in this process. However, to avoid reducing the yield in mass fabrication, it is generally not recommended, since hot lift-off and acetone/IPA baths already give good results in cleaning the chips. For additional cleaning, O_2 plasma etching can be used in case organic materials remain on the substrate. N_2 blow-drying is also not destructive, but gentle use is recommended at this stage, as IPA can easily dry with low power from the N_2 gun.

However, spin-coating resist on fabricated airbridges is completely destructive for the airbridges with the current design. This is critical in the ideal case where Josephson junctions are fabricated as the final step to avoid contamination or hot plate application on the junctions, which could increase their resistance. To address this issue, alternative designs, such as airbridges with stiffeners, thicker airbridges, or even Nb airbridges, can provide improved stability.

CHAPTER 5

Results

In this chapter, microwave measurements of the fabricated devices will be discussed. In total, three chips were measured. The first, AIR-1, contains only $\lambda/2$ resonators, which were used to extract the effective speed of light on the corresponding chip and to improve the design for the next generation. The second chip, AIR-2, contains $\lambda/4$ resonators and a transmission line. Lastly, AIR-3 includes grounded resonators with different numbers of airbridges, as well as bare resonators used for comparison.

The Oxford Instruments Triton refrigerator is used to perform cryogenic temperature experiments at around 17 mK, which ensures that Al and Nb thin films remain in their superconducting state and that thermal excitations are suppressed. The sample box, which contains the sapphire chip, is mounted on the base plate of the dilution refrigerator and is connected to the input lines via SMA ports. Incoming microwave signals are attenuated to reduce thermal and electrical noise before passing through the transmission line and interacting with the resonators. The transmitted signals are analyzed using a Vector Network Analyzer (VNA) by measuring the S_{21} transmission spectrum. Before reaching the VNA, the signal is amplified by a High Electron Mobility Transistor (HEMT) amplifier at the 4 K stage and again at room temperature.

5.1 Resonator Characterization

The signal passing through the transmission line interacts with the resonators while the frequency is swept by the VNA. At the resonance frequency, a dip is observed in S_{21} due to destructive interference between the incoming signal and the signal reflected by the resonator. The dip in magnitude $|S_{21}|$ at 3.771 GHz can be seen in Figure 5.1(a). The power applied by the VNA is reduced using a digital attenuator to allow the resonators to be measured at the single-photon level. The transmitted signal is then analyzed using a circle fit routine [43, 46] to extract resonator properties such as Q factors and resonance frequency.

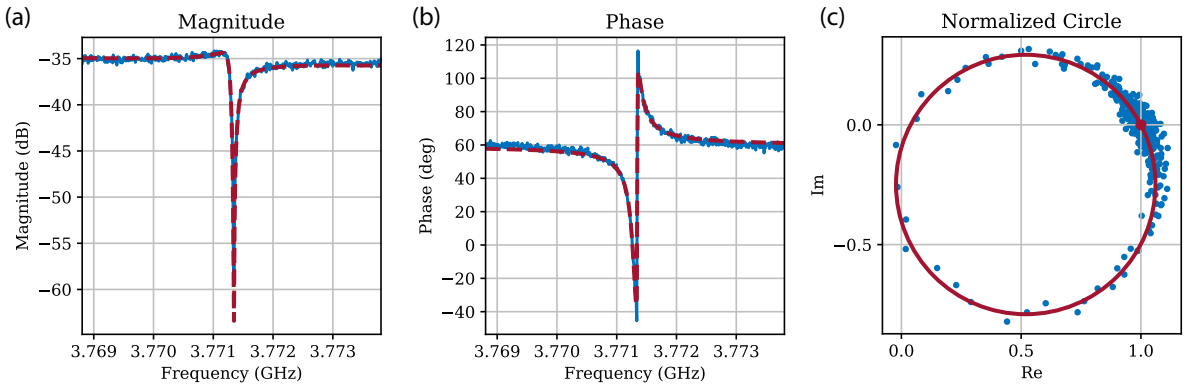

Fig. 5.1 (a–c) Magnitude, phase and normalized circle of the S_{21} transmission spectrum of a $\lambda/4$ CPW resonator. The extracted values for Q_l, Q_c and Q_{int} are 2.39×10^4, 2.48×10^4, and 6.20×10^5, respectively.

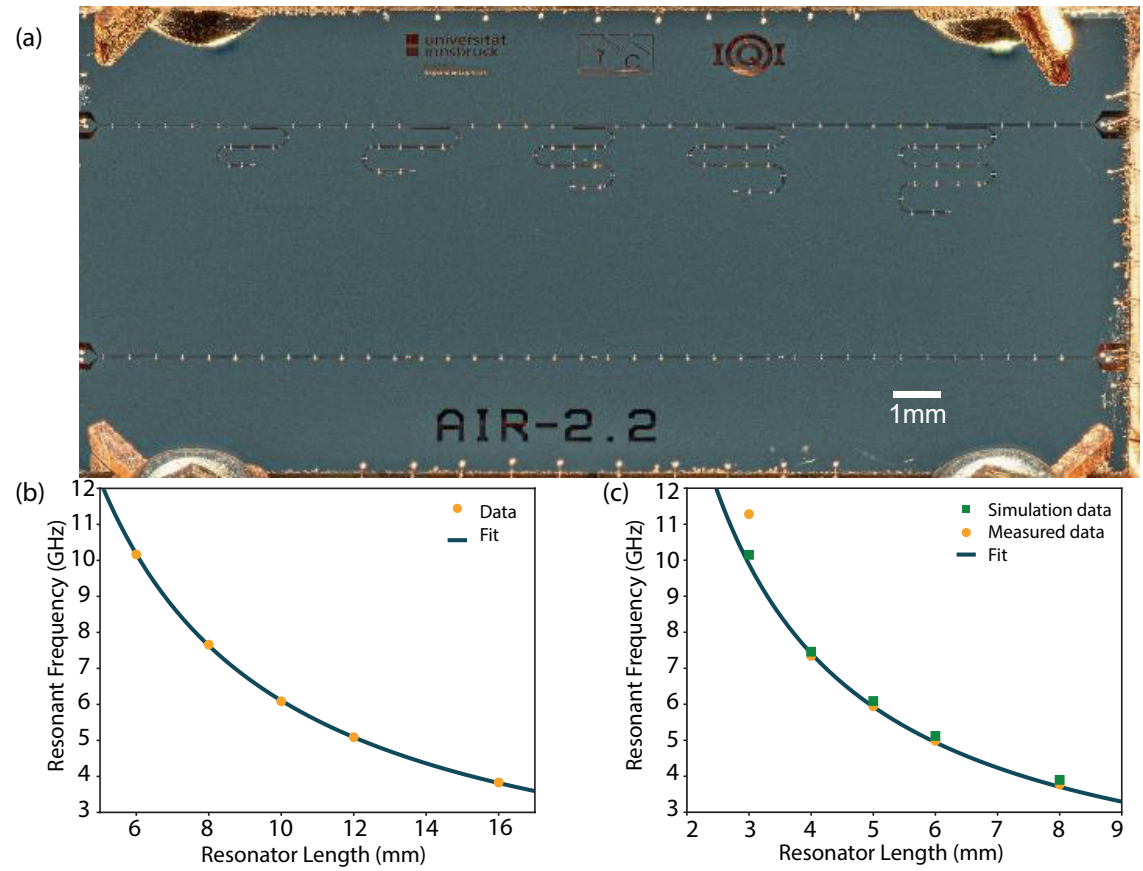

Fig. 5.2 (a) Overall chip of AIR-2. (b-c) Resonance frequencies of different lengths of $\lambda/2$ and $\lambda/4$ resonators are shown, respectively. All $\lambda/4$ resonators in (c) are designed to be half the length of the corresponding $\lambda/2$ resonators in (b) and each is shorted at the end with a single airbridge to convert it into a $\lambda/4$ resonator. Fit functions are $f_0 = \frac{c}{2l\sqrt{\varepsilon_{\text{eff}}}}$ and $f_0 = \frac{c}{4l\sqrt{\varepsilon_{\text{eff}}}}$, respectively. The ε_{eff} is the fit parameter.

The resonance frequency of the resonators depends on their length and the medium. The length of the resonators corresponds to either half or a quarter of the wavelength, depending on the boundary conditions: two open ends correspond to a $\lambda/2$ resonator, while one open end and one shorted end correspond to a $\lambda/4$ resonator. In Figure 5.2(a), the AIR-2 chip contains five resonators of various lengths, which are capacitively coupled to a transmission line. Their corresponding resonant frequencies are shown in Figure 5.2(c). The resonators are initially designed with two open ends, but one end is connected to the ground using a single airbridge (shorted), as shown in Fig 5.3(b). This electrical connection transforms the resonator into a $\lambda/4$ type. The $\lambda/2$ resonators in AIR-1, whose resonant frequencies are shown in Fig. 5.2(b). They were also redesigned in AIR-2 to be half of their original length. Without the airbridge connection, the resonant frequencies in AIR-2 would be expected to be twice those in AIR-1. However, the results show that the frequencies remain nearly the same. The slight difference observed is attributed to variations in different couplings of resonators, which affect the total capacitance, consequently, the resonant frequency. In addition, the simulation data and measured resonant frequencies match well, except at a resonator length of 3 mm, as shown in Fig. 5.2(c). This resonator was excluded from the fit since the frequency deviation is unexpected and may be due to fabrication errors. From the fit, the values of ϵ_{eff} for AIR-1 and AIR-2 were found to be 6.03 and 6.39, respectively, with corresponding phase velocities of 0.407 c and 0.396 c where the c is speed of light.

5.1.1 Quality factors

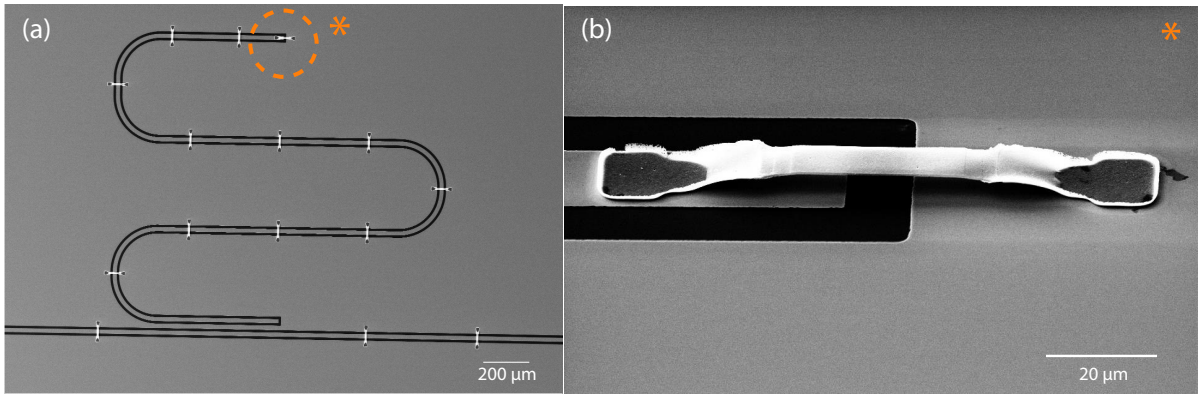

Fig. 5.3 (a) $\lambda/4$ resonators by connecting the center conductor and ground plane by one airbridge. (b) Detailed picture of dashed orange circle at (a).

After the transmitted signal is collected by the VNA, the complex value of S_{21} is recorded at different VNA power levels, which can be converted to the number of photons stored in the resonator. To perform low-power measurements around the single-photon level without being limited by the signal-to-noise ratio, the measurement is averaged multiple times.

In **AIR-2**, the internal quality factor is found to be approximately 6×10^5 at the single-photon level as can be seen in Fig.5.4. From this, it can be concluded that the airbridge electrical connection between the pedestals and the Nb ground layer is quite efficient, so that the internal quality factor is not significantly degraded.

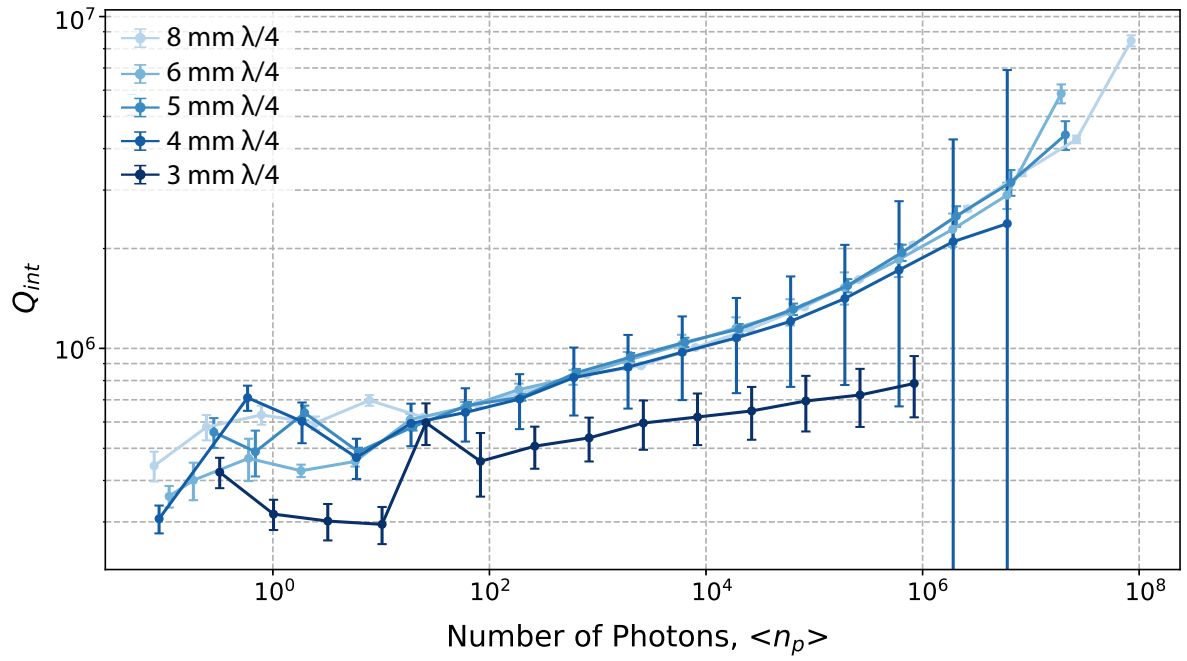

Fig. 5.4 Internal quality factors of the AIR-2 as a function of a number of photons.

Fig. 5.5 (a) Internal quality factor of AIR3 for different number of bridges. (b) Comparison of Q_{int} at approximately single-photon level for direct grounded and airbridge grounded $\lambda/4$ as seen in 5.3.

In the **AIR-3** chip, two transmission lines were fabricated. One line contains five resonators originally designed as $\lambda/4$, with 200 MHz frequency spacing to allow clear distinction in the S_{21} spectrum and each resonator is grounded using a different number of airbridges. Due to proximity effect considerations, the airbridges were placed with a minimum spacing of 80 μm, which corresponds to approximately 10% of the total resonator length. The other line includes

identical resonators without any airbridge grounding, which serve as test resonators. As shown in Figure 5.5, the internal quality factor Q_{int} at the single-photon level for AIR-3 is observed to be similar to that of AIR-2, indicating that airbridge connections do not introduce significant additional inductive loss. Furthermore, no correlation has been observed between Q_{int} and the number of airbridges, as seen in Figure 5.5(b).

However, the resonators on both chips operate in the overcoupled regime, with coupling quality factors Q_c around $1\text{–}2 \times 10^5$ for all resonators. This means that the total loss is dominated by external loss rather than by the internal properties of the resonators. The overcoupling regime also prevents precise determination of internal losses due to Fano interference [48]. Ideally, the resonators should be weakly coupled in order to efficiently quantify the loss contribution from each airbridge which will be considered in future designs.

To assess the mechanical stability against environmental vibrations, such as those of the pulse tube, measurements on AIR-2 were repeated with the pulse tube on and off. No differences in quality factor were detected.

5.2 Effect of Airbridges on Resonators

In contrast to crossovers supported by dielectrics, airbridges introduce less shunt capacitance to the resonator. However, since this additional capacitance is not negligible, it can be quantified using a parallel capacitance model. Specifically, the capacitance introduced by the airbridges contributes as a parallel component to the total capacitance of the resonator.

To measure the frequency shift caused by the airbridges, as shown in Fig. 5.6(a), resonators with varying numbers of airbridges were fabricated and coupled to the first transmission line. Each resonator is distinguished by a 200 MHz frequency spacing in the S_{21} measurement. On the second transmission line, we fabricated an identical geometry to the first one, but without any airbridges, to serve as a control resonator. Increasing the capacitance results in a decrease in the resonance frequency of the resonators grounded by airbridges. The frequency shift due to the airbridges is given by

$$\Delta f = f_{\text{bare}} - f_{\text{airbridged}} = \frac{1}{2\pi\sqrt{LC}} - \frac{1}{2\pi\sqrt{LC + \Delta(LC_n)}}. \tag{5.1}$$

Here, L and C are the total inductance and capacitance of the bare resonators, and $\Delta(LC_n)$ is the change in the LC product due to the airbridges. However, airbridges also introduce additional current paths, which effectively reduce the inductance. This reduction in inductance can partially compensate for the increase in capacitance [29]. Nonetheless, the inductive contribution of airbridges is difficult to quantify precisely, as edge effects play a significant role. The geometry and shape of the airbridges strongly influence their inductive impact. These factors make it challenging to extract the capacitance contribution of a single airbridge from the measurements, and therefore we determine only the total change in the LC product. The total change in LC can be expressed as

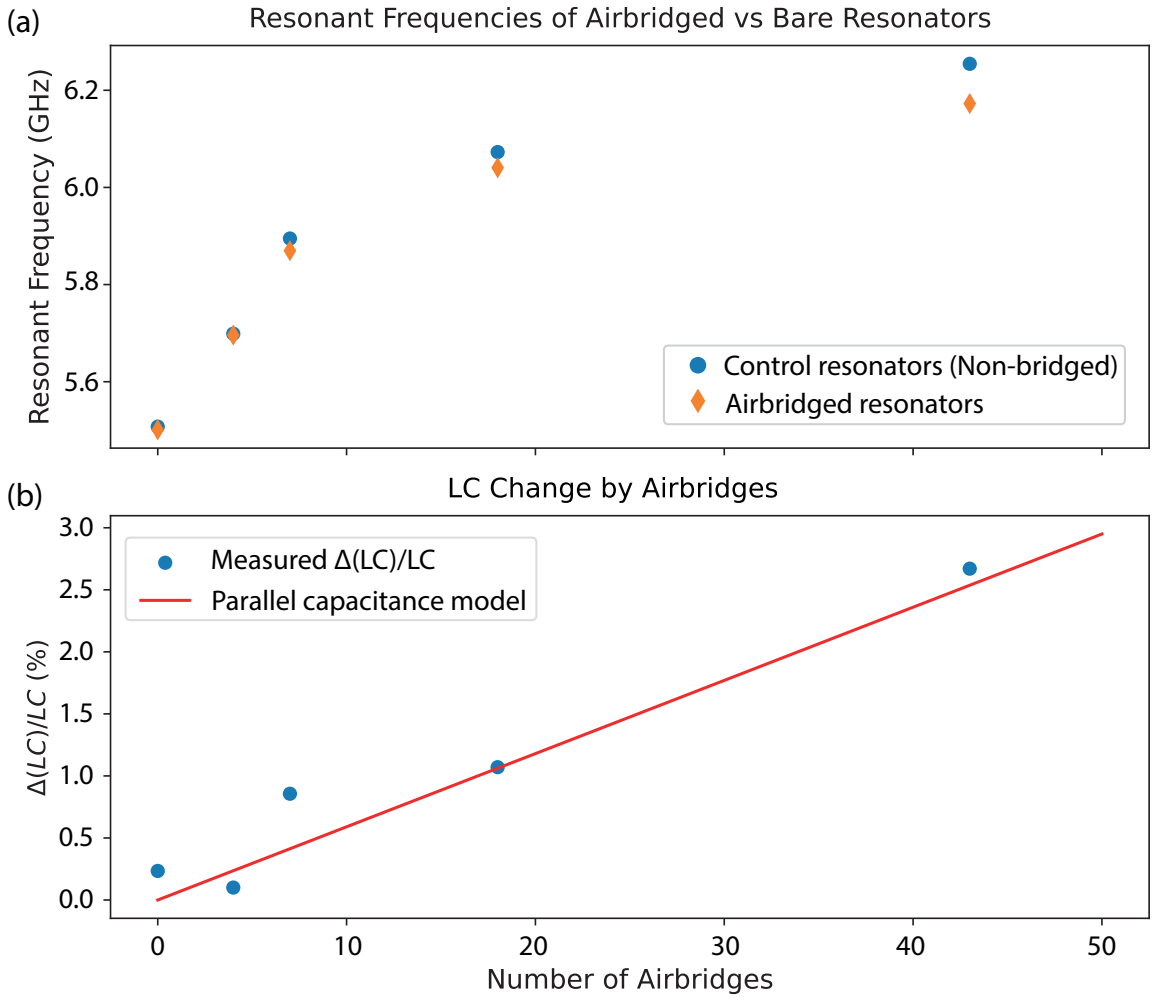

Fig. 5.6 (a) Frequency shift by airbridges on $\lambda/4$ resonators. (b) The percentage change in LC of resonators due to airbridges from measurements is shown with blue dots and the prediction from the parallel capacitance model is indicated by the red line.

$$\Delta(LC) = (LC)_{\text{airbridged}} - (LC)_{\text{bare}} = \frac{1}{(2\pi f_{\text{airbridged}})^2} - \frac{1}{(2\pi f_{\text{bare}})^2}. \tag{5.2}$$

From the measured resonant frequencies, we can obtain the ratio of the total change in inductance and capacitance due to airbridges, given by $\Delta(LC)/LC$, as shown in percentage in Fig. 5.6(b). Since the change in L is quite small, we can model the effect of airbridges using a parallel capacitance model. First, we will quantify the inductance and capacitance per unit length. In addition, the participation of the airbridges is not uniform along the CPW resonator because the standing-wave voltage varies with position. Therefore, we replace the bridge count n with an effective number n_{eff}. For airbridges evenly spaced along a $\lambda/4$ CPW, the effective count is

$$n_{\text{eff}} = n\,\frac{1}{\ell}\int_0^{\ell} \sin^2\!\left(\frac{\pi z}{2\ell}\right) dz = \frac{n}{2}.$$

The resonant frequency of the airbridged resonator can be written as

$$f_{\text{airbridged}} = \frac{1}{2\pi\sqrt{LC}} \cdot \frac{1}{\sqrt{1+\frac{\delta C}{C} n_{\text{eff}}}}. \tag{5.3}$$

Here, δC is the capacitance introduced by an airbridge and n is the number of the airbridge. It can be estimated as $\delta C = \frac{\varepsilon_0 A}{d}$, where A is the area of the center conductor covered by the airbridge (20 μm $\times$ 10 μm), and d is the height of the bridge, which is about 3.2 μm. Based on this model, the expected added capacitance per airbridge is approximately 0.553 fF. However, since the capacitance added by the airbridges is quite small compared to the total capacitance of the resonator, we can expand the frequency expression using a Taylor expansion, such as $\frac{1}{\sqrt{1+\epsilon}} \approx 1 - \frac{1}{2}\epsilon + \ldots$. The resonant frequency of the airbridged resonator is given by

$$f_{\text{airbridged}} \approx \frac{1}{2\pi\sqrt{LC}} \left[1 - \frac{1}{2}\left(\frac{\delta C}{C}\right) n_{\text{eff}}\right], \tag{5.4}$$

The frequency difference between the airbridged and bare resonators, as shown in equation 5.1, can be rewritten as

$$\Delta f = f_{\text{bare}} \cdot \frac{1}{2}\frac{\delta C}{C} n_{\text{eff}}. \tag{5.5}$$

Now we can express the total capacitance of the bare resonator in terms of known values and the capacitance per unit length is given[22]

$$C = \frac{1}{2}\frac{\delta C\, n_{\text{eff}}\, f_{\text{bare}}}{\Delta f}, \tag{5.6}$$

$$C' = \frac{2C}{l}. \tag{5.7}$$

From these expressions, we can calculate C and L from our measured values. Accordingly, the inductance per unit length and the total inductance are calculated as follows:

$$L' = \frac{1}{(4l)^2 C' f_{\text{bare}}^2}, \tag{5.8}$$

$$L = \frac{8L'l}{\pi^2}. \tag{5.9}$$

For the 5 mm resonator, which has a resonance frequency of 6.07 GHz without airbridges and 6.04 GHz with 18 airbridges, the capacitance and inductance of the bare resonator are found to be 0.469 pF and 1.465 nH, respectively. In addition, the inductance and capacitance per unit length are 361.4 nH/m and 187.6 pF/m, respectively. Using the online simulator [64], the expected L and C values for a 5 mm resonator are obtained as 1.57 nH and 0.43 pF, respectively. To apply the parallel capacitance model, we assume that L is not affected by the airbridges and

use the inductance of the 5 mm resonator as a reference. Under this assumption, $\Delta(LC)$ becomes

$$\Delta(LC) = L\Delta C. \tag{5.10}$$

Moreover, $L\Delta C/LC$ is plotted in Fig. 5.6(b). Since the extracted LC change from the measurement matches well with the model, this approach works for small added capacitances. For a much higher number of airbridges, where the added capacitance becomes more significant, one can use the second-order term of the Taylor expansion rather than equation 5.4.

5.3 Through Line

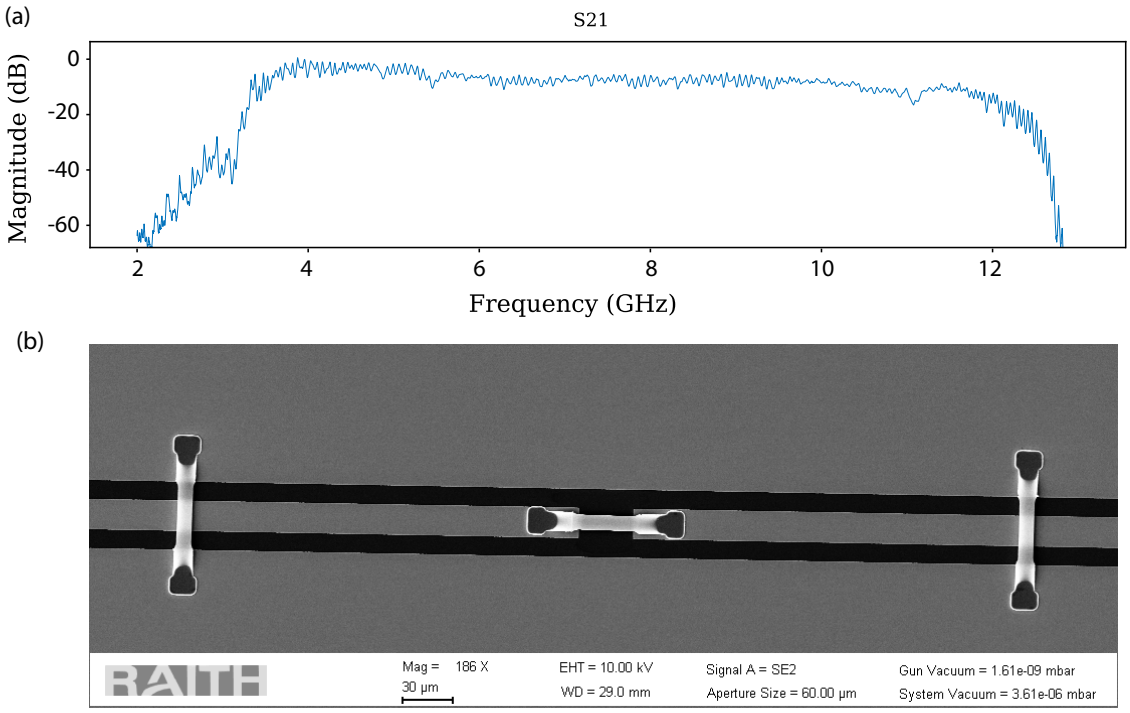

Fig. 5.7 (a) S_{21} transmission spectrum of CPW transmission line that is reconnected by an airbridge. The transmission line is disconnected intentionally and reconnected by an airbridge.

In some cases, when chip complexity increases, the CPW lines may need to cross each other, requiring the center trace to be temporarily disconnected. The airbridges enable the reconnection of two separated CPW sections, as shown in Figure 5.7(b) and one such transmission line with three intentional disconnections was fabricated on AIR-2. These gaps were bridged using airbridges. The RF signal was transmitted through the line and the S_{21} transmission spectrum was measured, as shown in Figure 5.7(a). In the transmission spectrum, no significant attenuation and excess ripples are observed, indicating that airbridges provide effective crossover connections.

Additionally, this test was repeated by applying a DC current of 560 μA to the transmission line. No noticeable change was observed in the transmission spectrum, confirming that the airbridges are mechanically and electrically robust enough to support efficient signal transmission without significant reflection, even under DC bias conditions.

CHAPTER 6

Conclusion and Outlook

In conclusion, Al airbridges were fabricated for the first time at QNZT during this thesis. Grayscale lithography using 30 keV EBL was improved through 3D proximity effect correction for single-step exposure. Delayed development or a post-exposure bake (PEB) was integrated into the fabrication process. Both delayed development and PEB helped to homogenize the development results, since the time between exposure and development plays an important role, especially in large-scale fabrication, where there is a time gap between the first and last exposed airbridge masks. Additionally, this process increases the usable dose range while improving control over the resist height, which is highly desirable in grayscale EBL. The process was successfully adapted for use on both Si and sapphire wafers.

The first consideration for airbridges was whether they could stand without a supportive layer at sufficient lengths. For the longest bridge, 85 μm, a yield of over 80% was achieved, while bridge lengths up to 65 μm showed a yield of over 99%. However, the yield may vary depending on the use of higher-power N_2 blow or additional ultrasonic baths. In general, bridges survived N_2 drying when applied gently after lift-off and were durable enough to withstand sonication if full power is avoided. However, they were not stable against resist spin-coating over the bridges. Ideally, the yield for longer bridges could be improved by modifying the design in the future. The currently achieved length of 65 μm is highly compatible with the present geometries of the CPW line.

Argon ion milling was employed in the process to improve the electrical connection between the airbridges and the ground plane. The efficiency of this contact was demonstrated by intentionally disconnecting a through-line and reconnecting it with a single airbridge, which resulted in no observable difference in the transmission spectrum. In addition, one end of a CPW resonator (initially designed with two open ends) was shorted by an airbridge and a corresponding frequency conversion was observed. An aluminum layer with a thickness of 450 nm was used for the airbridges and deposited using planetary evaporation. However, triangular evaporation has

also been proposed for greater mechanical stability, although it introduces design complexity and angle dependency [31].

CPW resonators were also designed and fabricated with airbridges. The fabricated airbridged resonators were measured in a cryogenic environment and the internal quality factors Q_{int} were found to be around 5×10^5, which is slightly lower than current values reported in the literature [23] at the single-photon level. However, these internal quality factors are not entirely reliable, as the resonators are overcoupled. Due to being in an overcoupled regime, the loss per airbridge cannot be accurately determined, since external losses dominate over internal losses. In future design, the resonator design will be modified to operate in the undercoupled regime, allowing the loss per airbridge to be properly quantified.

In the next steps, the single-step airbridge fabrication process will be adapted to different materials such as Nb and Ta. Both Nb and Ta have higher critical temperatures and greater durability in the thin-film form, which can enhance the mechanical stability of airbridges, especially for longer bridges. In addition, this increased stability may enable resist spinning over airbridges, which is an important capability, as airbridges are currently fabricated as the final step in superconducting qubit chips. This ordering is required because the airbridge process may alter the characteristics of the Josephson junctions. Some attempts have been made to fabricate airbridges with Nb in the current fabrication method, but the high temperature required for Nb evaporation has made it difficult to deposit the same thickness as with Al. This issue could potentially be addressed by evaporating a protective Al layer on top of the resist, which would help prevent thermal stress and burn both the thin film and the resist mask.

Bibliography

1. Janzen, N., Kononenko, M., Ren, S. & Lupascu, A. Aluminum air bridges for superconducting quantum devices realized using a single-step electron-beam lithography process. *Applied Physics Letters* **121,** 094001 (2022).
2. Mortelmans, T. *et al.* Grayscale e-beam lithography: Effects of a delayed development for well-controlled 3D patterning. *Microelectronic Engineering* **225,** 111272 (2020).
3. Shao, J. *et al.* Y shape gate formation in single layer of ZEP520A using 3D electron beam lithography. *Microelectronic Engineering* **143,** 37–40 (2015).
4. Feynman, R. P. Simulating physics with computers. *International journal of theoretical physics* **21,** 467–488 (1982).
5. Kielpinski, D., Monroe, C. & Wineland, D. J. Architecture for a large-scale ion-trap quantum computer. *Nature* **417,** 709–711 (2002).
6. Nakamura, Y., Pashkin, Y. A. & Tsai, J. Coherent control of macroscopic quantum states in a single-Cooper-pair box. *nature* **398,** 786–788 (1999).
7. Peruzzo, A. *et al.* A variational eigenvalue solver on a photonic quantum processor. *Nature communications* **5,** 4213 (2014).
8. Arute, F. *et al.* Quantum supremacy using a programmable superconducting processor. *Nature* **574,** 505–510 (2019).
9. Krinner, S. *et al.* Realizing repeated quantum error correction in a distance-three surface code. *Nature* **605,** 669–674 (2022).
10. Gottesman, D. *Stabilizer Codes and Quantum Error Correction* 1997. arXiv: `quant-ph/9705052 [quant-ph]`.
11. Shor, P. W. Scheme for reducing decoherence in quantum computer memory. *Physical review A* **52,** R2493 (1995).
12. Cerezo, M. *et al.* Variational quantum algorithms. *Nature Reviews Physics* **3,** 625–644 (2021).
13. Jazaeri, F., Beckers, A., Tajalli, A. & Sallese, J.-M. *A review on quantum computing: From qubits to front-end electronics and cryogenic MOSFET physics* in *2019 MIXDES-26th International Conference" Mixed Design of Integrated Circuits and Systems"* (2019), 15–25.
14. Huang, H.-L., Wu, D., Fan, D. & Zhu, X. Superconducting quantum computing: a review. *Science China Information Sciences* **63,** 1–32 (2020).
15. Preskill, J. Quantum computing in the NISQ era and beyond. *Quantum* **2,** 79 (2018).

16. Zhang, J. *et al.* Observation of a many-body dynamical phase transition with a 53-qubit quantum simulator. *Nature* **551,** 601–604 (2017).

17. Wallraff, A. *et al.* Strong coupling of a single photon to a superconducting qubit using circuit quantum electrodynamics. *Nature* **431,** 162–167 (2004).

18. Wallraff, A. *et al.* Approaching unit visibility for control of a superconducting qubit with dispersive readout. *Physical review letters* **95,** 060501 (2005).

19. Majer, J. *et al.* Coupling superconducting qubits via a cavity bus. *Nature* **449,** 443–447 (2007).

20. Frunzio, L., Wallraff, A., Schuster, D., Majer, J. & Schoelkopf, R. Fabrication and characterization of superconducting circuit QED devices for quantum computation. *IEEE transactions on applied superconductivity* **15,** 860–863 (2005).

21. Barends, R. *et al.* Niobium and tantalum high Q resonators for photon detectors. *IEEE transactions on applied superconductivity* **17,** 263–266 (2007).

22. Göppl, M. *et al.* Coplanar waveguide resonators for circuit quantum electrodynamics. *Journal of Applied Physics* **104,** 113904 (2008).

23. Drimmer, M. *et al.* The effect of niobium thin film structure on losses in superconducting circuits. *arXiv preprint arXiv:2403.12164* (2024).

24. Houck, A. A. *et al.* Controlling the spontaneous emission of a superconducting transmon qubit. *Physical review letters* **101,** 080502 (2008).

25. Harokopus, W. & Katehi, P. *Radiation loss from open coplanar waveguide discontinuities* in *1991 IEEE MTT-S International Microwave Symposium Digest* (1991), 743–746.

26. Wenner, J. *et al.* Wirebond crosstalk and cavity modes in large chip mounts for superconductingqubits. *Superconductor Science and Technology* **24,** 065001 (2011).

27. Sun, Y. *et al.* Fabrication of airbridges with gradient exposure. *Applied Physics Letters* **121,** 074001 (2022).

28. Abuwasib, M., Krantz, P. & Delsing, P. Fabrication of large dimension aluminum airbridges for superconducting quantum circuits. *Journal of Vacuum Science & Technology B* **31,** 031601 (2013).

29. Chen, Z. *et al.* Fabrication and characterization of aluminum airbridges for superconducting microwave circuits. *Applied Physics Letters* **104,** 052602 (2014).

30. Jin, Y. *et al.* Microscopic metallic air-bridge arrays for connecting quantum devices. *Applied Physics Letters* **118,** 162108 (2021).

31. Tao, H.-R. *et al.* Fabrication and characterization of low loss niobium airbridges for superconducting quantum circuits. *Applied Physics Letters* **125,** 034001 (2024).

32. Bolgar, A. N. *et al.* Highly stable aluminum air-bridges with stiffeners. *Journal of Applied Physics* **137,** 154401 (2025).

33. Girgis, E., Liu, J. & Benkhedar, M. Fabrication of metallic air bridges using multiple-dose electron beam lithography. *Applied physics letters* **88,** 202103 (2006).

34. Stavenga, T., Khan, S., Liu, Y., Krogstrup, P. & DiCarlo, L. Lower-temperature fabrication of airbridges by grayscale lithography to increase yield of nanowire transmons in circuit QED quantum processors. *Applied Physics Letters* **123,** 024004 (2023).

35. Bu, K. *et al.* Tantalum airbridges for scalable superconducting quantum processors. *npj Quantum Information* **11,** 17 (2025).
36. Bardeen, J., Cooper, L. N. & Schrieffer, J. R. Theory of superconductivity. *Physical review* **108,** 1175 (1957).
37. Van Delft, D. & Kes, P. The discovery of superconductivity. *Physics today* **63,** 38–43 (2010).
38. Koizumi, H. & Ishikawa, A. Theory of supercurrent in superconductors. *International Journal of Modern Physics B* **34,** 2030001 (2020).
39. Romijn, J., Klapwijk, T., Renne, M. & Mooij, J. Critical pair-breromijn1982criticalaking current in superconducting aluminum strips far below T c. *Physical Review B* **26,** 3648 (1982).
40. Kupriyanov, M. Y. & Lukichev, V. Temperature dependence of pair-breaking current in superconductors. *Soviet Journal Low Temperature Physics* **6,** 210–214 (1980).
41. Pozar, D. M. *Microwave Engineering: Theory and Techniques* 2nd, 65–70 (John Wiley & Sons, 1998).
42. Pozar, D. M. *Microwave Engineering: Theory and Techniques* 2nd, 196–198 (John Wiley & Sons, 1998).
43. Zöpfl, D. *Characterisation of Stripline Resonators in a Waveguide* Supervisor: Univ.-Prof. Dr. Gerhard Kirchmair. M.Sc. thesis (Institute of Experimental Physics, University of Innsbruck, Innsbruck, Austria, Apr. 2017). `https://kirchmair.iqoqi.at/images/group/gk/master-theses/characterisation-of-stripline-resonators-in-a-waveguide.pdf`.
44. Reagor, M. J. *Superconducting Cavities for Circuit Quantum Electrodynamics* Dissertation Director: Professor Robert J. Schoelkopf. PhD thesis (Yale University, New Haven, Connecticut, USA, Dec. 2015). `https://rsl.yale.edu/sites/default/files/2024-08/2016-RSL-Thesis-Matt-Reagor.pdf`.
45. Meier, S. *Loss reduction of superconducting coplanar microwave resonators on sapphire substrates* Supervisor: Prof. Dr. Rudolf Gross. Munich, Germany, Aug. 2014. `https://www.wmi.badw.de/fileadmin/WMI/Publications/Meier%2CSebastian%20Bachelor%20Thesis%202014.pdf`.
46. Probst, S., Song, F., Bushev, P. A., Ustinov, A. V. & Weides, M. Efficient and robust analysis of complex scattering data under noise in microwave resonators. *Review of Scientific Instruments* **86,** 024706 (2015).
47. Ansoft. *User's Guide – High Frequency Structure Simulator* Version 10 (2005). `https://anlage.umd.edu/HFSSv10UserGuide.pdf`.
48. Rieger, D. *et al.* Fano interference in microwave resonator measurements. *Physical Review Applied* **20,** 014059 (2023).
49. Read, A. P. *et al.* Precision measurement of the microwave dielectric loss of sapphire in the quantum regime with parts-per-billion sensitivity. *Physical Review Applied* **19,** 034064 (2023).
50. Bal, M. *et al.* Systematic improvements in transmon qubit coherence enabled by niobium surface encapsulation. *npj Quantum Information* **10,** 43 (2024).
51. Su, F. *et al.* Fabrication and characterization of superconducting multiqubit device with niobium base layer. *Chinese Physics B* **30,** 100304 (2021).

52. Sharma, E. *et al.* Evolution in lithography techniques: microlithography to nanolithography. *Nanomaterials* **12,** 2754 (2022).

53. Pimpin, A. & Srituravanich, W. Review on micro-and nanolithography techniques and their applications. *Engineering journal* **16,** 37–56 (2012).

54. Materials, K. A. *Positive vs. Negative Tone Photoresists* https://kayakuam.com/products/lithography-overviews/.

55. Rius, G. *Electron Beam Lithography for Nanofabrication* Supervisors: Pr. Francesc Pérez-Murano and Pr. Joan Bausells Roigé. Ph.D. thesis (Universitat Autònoma de Barcelona, Barcelona, Spain, 2008), 18. https://www.tdx.cat/bitstream/handle/10803/3404/grs1de2.pdf.

56. Murali, R., Brown, D. K., Martin, K. P. & Meindl, J. D. Process optimization and proximity effect correction for gray scale e-beam lithography. *Journal of Vacuum Science & Technology B: Microelectronics and Nanometer Structures Processing, Measurement, and Phenomena* **24,** 2936–2939 (2006).

57. Lake, J. H., Cambron, S. D., Walsh, K. M. & McNamara, S. Maskless grayscale lithography using a positive-tone photodefinable polyimide for MEMS applications. *Journal of microelectromechanical systems* **20,** 1483–1488 (2011).

58. Rogers, J. D., Kärkkäinen, A. H., Tkaczyk, T., Rantala, J. T. & Descour, M. R. Realization of refractive microoptics through grayscale lithographic patterning of photosensitive hybrid glass. *Optics Express* **12,** 1294–1303 (2004).

59. Wu, C. S., Makiuchi, Y. & Chen, C. in *Lithography* (ed Wang, M.) chap. 13 (IntechOpen, Rijeka, 2010). https://www.intechopen.com/chapters/8670.

60. Bolten, J. *et al.* Improved CD control and line edge roughness in E-beam lithography through combining proximity effect correction with gray scale techniques. *Microelectronic engineering* **87,** 1041–1043 (2010).

61. Madou, M. J. *Manufacturing techniques for microfabrication and nanotechnology* 25–27 (CRC press, 2011).

62. HORIBA Scientific. *Cauchy and Related Empirical Dispersion Formulae for Transparent Materials* tech. rep. Technical Note, available at https://www.horiba.com/fileadmin/uploads/Scientific/Downloads/OpticalSchool_CN/TN/ellipsometer/Cauchy_and_related_empirical_dispersion_Formulae_for_Transparent_Materials.pdf (HORIBA Scientific, n.d.).

63. Stout, V. L. & Gibbons, M. D. Gettering of gas by titanium. *Journal of applied physics* **26,** 1488–1492 (1955).

64. Boutell, T. *Coplanar Waveguide Analysis/Synthesis Calculator* http://wcalc.sourceforge.net/cgi-bin/coplanar.cgi. 2009.

APPENDIX A

Fabrication Recipe

Fabrication steps	Details
Wafer cleaning	5 min in hot acetone and 5 min in isopropanol with ultrasonication
Resist spinning	PMMA in 11% anisole at 500 rpm for 5 s and 1250 rpm for 60 s
Baking	3 min on a 150 °C hot plate
Resist spinning	Electra at 2000 rpm for 100 s
Baking	2 min on a 90 °C hot plate
E-beam lithography	Gradient exposure dose from 60 µC/cm^2 to 275 µC/cm^2 at 30 kV acceleration voltage
Post-exposure bake or delay	72 h delay between exposure and development, or 20 min on a 45 °C hot plate
Etching Electra	H_2O for 60 s
Development	20 s in MIBK at 22 °C
Rinse and dry	30 s in IPA and blow dry with N_2
Reflow the resist	1 min on a 130 °C hot plate
Ion milling and gettering	1 min Ar milling (400 V beam, 80 V acceleration, 22 mA beam current, 40 V discharge) and 2 min Ti gettering at 0.2 nm/s (chamber pressure $< 10^{-7}$ mbar)
Al evaporation	450 nm Al deposition at 1 nm/s
Al etching	Transene Al Etchant Type A for 180 s
Dicing and lift-off	Dicing with laser dicer and lift-off in AR672.11 at 65 °C for at least 2 h
Rinse and dry	Rinse in IPA and gently blow dry with N_2

Tab. A.1 Fabrication recipe of Al airbridges.